THE UNIVERSITY
OF ADELAIDE
AUSTRALIA

Guiding Light in Low-Index Media via Multilayer Waveguides

by

Kristopher J. Rowland

Supervisors:
Prof. Tanya M. Monro
Dr Shahraam Afshar Vahid

A thesis submitted in fulfillment of the
degree of Doctor of Philosophy

in the
Faculty of Sciences
School of Chemistry & Physics

December 2010

Chapter 3

Bragg-Cladding Waveguides; Antiresonance, Reflectance and Bandgap Phenomena

THIS chapter focuses on two themes: reconciliation of antiresonance, reflectance and bandgap phenomena for guidance in depressed-core waveguides with binary 1D-periodic claddings (*e.g.*, Fig. 3.1); and from this, construction of the SPARROW model—a simple analytic model for the analysis of the nontrivial antiresonance, reflectance and bandgap spectra of such structures on and *below* the low-index light line ($\tilde{n} < n_0$).

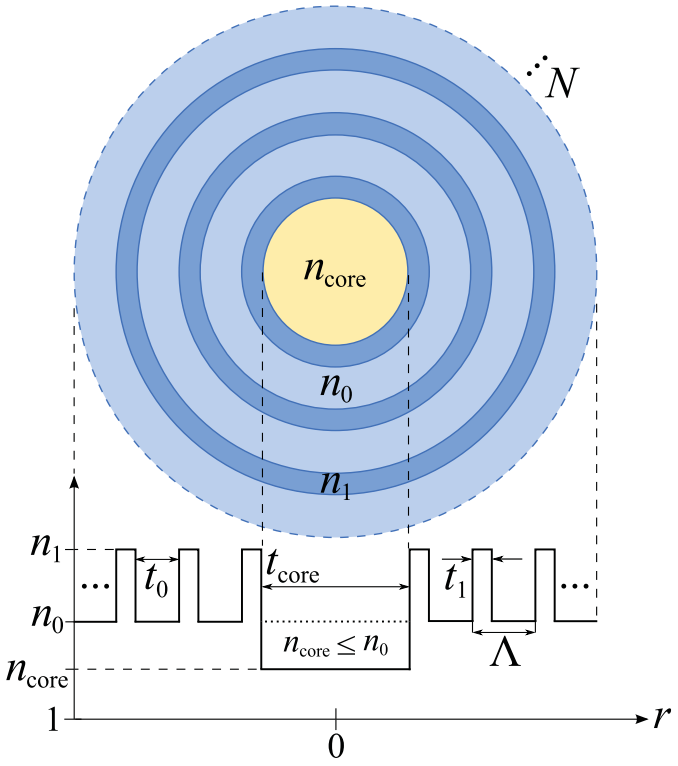

FIGURE 3.1: Schematic representation of a depressed-core Bragg fibre. All parameters are defined within. Refractive indices take any value such that $1 \leq n_{\text{core}} \leq n_0 < n_1$.

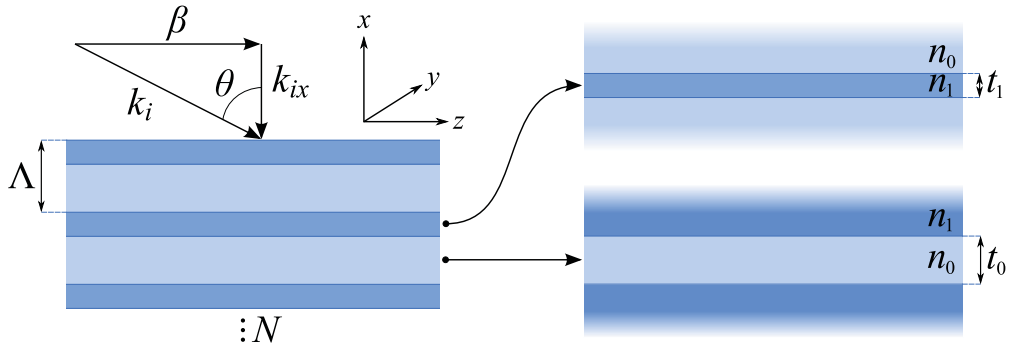

FIGURE 3.2: *Left:* The equivalent planar slab representation of the Bragg-cladding of Fig. 3.1 with N layers of alternating high- and low-index. *Right:* The planar layers of the stack considered in isolation. The vector diagram represents the decomposition of an incident ray's wavevector. High-index layers (dark blue) have refractive index n_1 and thickness t_1 and low-index layers (light blue) have refractive index $n_0 < n_1$ and thickness t_0.

This chapter is an extension of a publication compiled within the duration of research for this Thesis: Kristopher J. Rowland, Shahraam Afshar V. and Tanya M. Monro, 'Bandgaps and antiresonances in integrated-ARROWS and Bragg fibers; a simple model', Optics Express, Vol. 16, Issue 22, pp. 17,935-17,951 (16 pages in total), published October 21, 2008—co-published in *The Virtual Journal for Biomedical Optics*, Vol. 3, Issue 12, December 1, 2008.

This chapter is somewhat of an extension on Chapter 2 in that it generalises the analysis now to depressed-core waveguides, not just level-core. By making the core refractive index a free parameter, a wealth of extra phenomena can be considered. This chapter goes some way to understand such phenomena using a variety of theoretical techniques, from analytic to numerical models.

Considering the first theme, fibres with a binary layered cladding, Bragg fibres, are well known for their ability to confine light to cores with refractive indices equal to or lower than either of the cladding indices (*e.g.*, Temelkuran et al. [41]). A schematic representation of a depressed-core Bragg fibre is shown in Fig. 3.1. Analogous types of planar waveguides known as Integrated Antiresonant Reflecting Optical Waveguides, I-ARROWs, exhibit similar low-index confinement behaviour but are typically treated as distinct to Bragg waveguides and their associated bandgap guidance mechanism (*e.g.*, Yin et al. [26]). A schematic representation of an I-ARROW with rectangular and arch shaped profiles was shown in Fig. 1.3. Bragg fibres and I-ARROWs, their concepts, fabrication methods, examples and applications were discussed in § 1.2.2.

A Bragg waveguide cladding (Fig. 3.1) can be approximated as an infinite 1-D Bragg stack (Fig. 3.2), a photonic crystal, such that the behaviour of the supported Bloch modes dictates whether light can or can not couple to the cladding [34, 36–42, 44]: core

modes exist only for wavelengths and propagation constants that fall within the Bloch modes' forbidden regions (bandgaps).

ARROW guidance, on the other hand, is typically attributed to the antiresonance of light with the cladding layers considered in isolation (Fig. 3.2) as waveguides in their own right [99–102, 173, 174]: light will preferentially be coupled into a particular layer at the layer's resonant frequencies, such that the transverse component of the light wave interferes constructively with itself for each round trip within the layer; light at wavelengths sufficiently far from the cladding resonances will be confined to the core due to restricted coupling (antiresonance) with the cladding layers themselves. In this sense, the layers act as Fabry-Perot cavities [14], reflecting light not satisfying its resonant conditions back into the core.

Both the bandgap and antiresonance mechanisms were discussed in detail in §§ 1 and (in particular for the 1-D case) 2. The critical distinction for the work in this section is that I am concerned with guidance *below* the low-index light-line ($\tilde{n} \geq n_0$). Much of the literature discussed in earlier chapters considers antiresonance on (or above) the low-index light-line $\tilde{n} \geq n_0$ [9, 99–102, 143, 173]. In other words, the analyses were limited to the bound mode cut-off ($\tilde{n} = n_0$, § A.2.1.3) of the modes supported in the high-index cladding inclusions.

Here I suggest that the distinction between Bragg-cladding waveguides and integrated-ARROWs is somewhat artificial, with the only difference being semantic: whether the cladding has many ('Bragg') or few ('ARROW') cladding layers. Indeed, with hollow-core integrated-ARROWs now being considered with multiple cladding unit cells [26, 57, 188] this distinction begins to disintegrate. Thus, since these two waveguide structures are for all intents and purposes the same, it is natural to expect a strong relationship between the mechanism to which guidance in each waveguide is attributed: a relationship between the bandgap and antiresonance guidance mechanisms themselves. I explore this idea within by analysing and comparing the antiresonance and bandgap phenomena directly. In doing so, I develop a general antiresonance model for the $\tilde{n} \leq n_0$ regime; that is, for guidance *below* the high-index cladding layer mode cut-off condition.

It is useful here to highlight an important misnomer regarding the use of the term 'ARROW'. As it was initially conceived, the model used to describe ARROWs typically assumed that one of the cladding layer refractive indices was much greater than the core and remaining cladding index [173]. As such, many ARROW designs have a core index *equal* to the lowest of the cladding indices [99, 101, 102, 173, 194–196]; as defined earlier, for clarity I call these *level-core* waveguides. Indeed, this line of thought saw the ARROW model successfully applied to photonic crystal fibres with a 2-D cladding lattice structure and has spawned much interest in what have been termed 'ARROW

fibres': PCFs of a low-index substrate with a cladding of high-index rods (typically on, but not restricted to, a hexagonal lattice), as discussed in § 1.2.3. It is implicitly assumed that such fibres have a core refractive index equal to the surrounding low-index substrate, just like the early (level-core) ARROWs, and rightly so since it is structurally the only possibility for a 2-D cladding of isolated inclusions embedded in a substrate. For level-core waveguides, with either 1-D (layers or rings) or 2-D (lattice-based) cladding structures, the predominant antiresonance behaviour comes from the high-index inclusions alone with little dependence on their spacing (§ 1.2.3).

The general definition of an ARROW by Archambault et al. [174], however, dictates that the core index can have *any value up to* that of the lowest cladding index, provided both the resonances of the high- *and* low-index layers are considered; I will call these *depressed-core* waveguides, as defined in 1. *All* cladding layer resonances in depressed-core waveguides influence the spectral behaviour of the core modes [174], not just the high-index layer resonances. Indeed, it is the Archambault-ARROW model that is considered for most current work on integrated hollow-core ARROWs [26, 28, 56, 57, 197]. It would seem that this disparity between the use of the general depressed-core compatible Archambault-ARROW model as applied to I-ARROWS and its restricted level-core Duguay-ARROW [173] form as applied to PCFs ('ARROW fibres') is responsible for the apparent bifurcation of the use of the ARROW principle in the integrated-waveguide and fibre fields. This is most clearly demonstrated (to the best of the Author's knowledge) by the absence of antiresonance analyses for depressed-core Bragg fibres and the absence of a Bloch analyses for Integrated-ARROWs[1]; the two waveguide structures being fundamentally similar (depressed core, binary layered cladding), as discussed. The work presented here clearly demonstrates how both the antiresonance and bandgap principles are applicable to any depressed-core waveguide with a binary stratified cladding, particularly for fibres and integrated waveguides respectively.

Developed within is a generalised version of the Archambault-ARROW model[2], discussed presently, and it is used to demonstrate an intimate relationship between the bandgap and antiresonance guidance mechanisms associated with stratified cladding waveguides[3]. This new model is coined the *Stratified Planar* Anti-Resonant Reflecting Optical Waveguide (SPARROW) model to distinguish it from both the Archambault-ARROW model [174] and, in particular, the more restrictive level-core ARROW and ARROW fibre applications based on the Duguay-ARROW model [99, 101, 102, 173].

[1] A recent publication by Hawkins et al. [56] actually mentions the importance of a Bloch analysis but, similarly for most of the I-ARROW literature (to the best of my knowledge), does not make a deep connection between the Bloch analysis and antiresonance or use it for the design of such waveguides.

[2] The SPARROW model presented here, however, was actually developed without knowledge of the Archambault-ARROW model, discovering its existence only after deeper investigation of the literature.

[3] Something which the Archambault-ARROW model can not do due to an implicit inclusion of the core phase condition—discussed below

Indeed, as will be shown later (§ 3.7.3), the Duguay-ARROW model is a special case of the SPARROW model, found by enforcing a level-core index profile $\tilde{n} = n_0$. Critically, it will be demonstrated how both high- *and* low-index cladding layer resonances must be considered together for the most general waveguide analysis and design. Often (and, to the best of my knowledge, exclusively), the current I-ARROW literature employs the Archambault-ARROW model to optimise the layer properties independently from one another (*e.g.*, Ref. [57, 174, 197]); the following results using the SPARROW model will demonstrate why, especially for higher-order bandgaps/antiresonances, this is an incorrect approach.

This leads to the second major theme of this chapter. As shown in § 2.5, air-Bragg fibres [43, 147, 188] exhibit a class of large bandwidth bandgaps, whose higher-order gaps can exhibit interesting properties such as orders-of-magnitude lower loss (as per Chapter 2 and the subsequent publication, Rowland et al. [147]). Importantly, this analysis also demonstrated that such cladding structures produce bandgap spectra with rich 2-D [effective mode index vs. frequency—$(\tilde{n}, \Lambda/\lambda)$] structure below the light-line of the lowest-index cladding layer [147]. These gaps are distinct from, yet related to, the gaps typically studied in more conventional hollow-core/solid-cladding Bragg fibres [41, 42, 171] which lie far from the low-index light-line.

Here the resonances of the individual cladding high- and low-index layers are examined via the SPARROW model. By using multi-layer reflectance analysis, a connection is made between this generalised antiresonance model of individual layers and the Bloch bandgap spectra of the infinite layer stack equivalent. In doing so, an analytical physical description of the aforementioned nontrivial bandgap properties is derived. It will be demonstrated how how this model can determine a number of nontrivial bandgap and antiresonance properties with simple, fully analytic, expressions.

Modelling microstructured waveguides typically relies heavily on often cumbersome numerical analyses of the full waveguide structures to determine the guidance characteristics, highlighting the need for simpler models. While a Bloch-wave analysis may be used (and is throughout this work) on 1-D approximations to the cladding of a Bragg-cladding waveguide [36, 41–44, 147, 171], it is difficult to use the resultant semi-analytic bandgap condition [36] to glean the direct physical insight into the relationship between the cladding parameters and the bandgap spectra's structure and topology that comes with analytic forms. Such analytic tools are indispensable for the understanding and design of depressed-core layered-cladding waveguides, whether they be fibres (multi-dielectric, such as hollow-core Bragg fibres [41, 42, 171], or single-material air-Bragg fibres [43, 147, 188]) or Integrated-ARROWs [26, 28, 70, 174, 197]. It is thus expected that the SPARROW model will be particularly useful for the design of layered-cladding

waveguides with gas, liquid or solid cores for applications in such areas as sensing, microfluidics, nonlinear optics, particle manipulation and waveguide lasers.

3.1 Chapter Structure and Overview

The following sections are predominantly concerned with the development of the Stratified Planar Anti-Resonant Reflecting Optical Waveguide model and its application to exposing the interrelationships between and analysis of the antiresonance, reflectance and bandgap behaviour of 1-D binary layered media, in particular for depressed-core waveguides. Section 3.3 discusses the relevant background theory on antiresonances, planar guidance and multilayer reflectance in 1-D structures—bandgaps in 1-D structures have already been covered in the § 2.3.2. The dispersion characteristics of high- and low-index slab waveguides are discussed in § 3.3.2 and are used to formally define the SPARROW model in § 3.4. The expressions fundamental to the SPARROW model are the dispersion curves of the cladding layers considered in isolation (§ 3.3.2), giving the wavelengths and modal effective indices at which light preferentially couples to the cladding (resonances); avoiding these cladding resonances decreases the core-mode loss (antiresonance).

A thorough theoretical analysis (using the pTMM theory of § 3.3.3) of the multilayer reflectance of a structure considered in the text is presented; analytical derivations of the conditions for antiresonance behaviour for one (§ 3.5.1) or two (§ 3.5.2) layers, and physical insight born from it, is demonstrated using the pTMM formalism. The evolution from an antiresonance regime into a bandgap regime as increasing numbers of layers are added to the system is them discussed in § 3.5.3, again employing the pTMM reflectance analysis.

The SPARROW model's ability to predict high- and low-loss wavelengths is confirmed via a numerical example in § 3.6 where it is made clear that *both* the high- and low-index layer resonances must be taken into account in order to describe the chosen region of the 2-D bandgap spectrum. This follows directly from the definition of the *antiresonance mean point* (§ 3.7.2) which explicitly accommodates this behaviour. As mentioned, further analysis of the curve interactions (§ 3.7) leads to expressions describing nontrivial properties of the associated bandgaps, such as: the positions of all bandgap closure points and, from them, a consistent nomenclature for arbitrary bandgap spectra (§ 3.7.1); the *central antiresonance point* (§ 3.7.4)—a special case of the antiresonance mean point; and a quantitative measure of the topology of arbitrary bandgap spectra—the number of gaps within a specific domain (§ 3.7.5). Concluding remarks are given in § 3.8.

3.2 Fibre Parameters

The general structure considered here is that of a depressed-core Bragg fibre, as depicted in Fig. 3.1, and the equivalent 1-D planar stack based on the cladding, as depicted in Fig. 3.2. The fibre parameters are defined exactly as in § 2.2 except that here the core has a variable refractive index such that $n_{\text{core}} \leq n_0$. Namely:

$$n(r) = \begin{cases} n_{\text{core}} \leq n_0 & \text{for} \quad 0 < r < r_0 \\ n_i & \text{for} \quad r_{i-1} < r < r_i \quad \text{and} \quad i = 1 \rightarrow N \\ n_1 & \text{for} \quad r > r_N \end{cases}$$

where all even or odd numbered rings have the same refractive index n_i and thickness $t_i = r_i - r_{i-1}$, allowing one to define $n_i = \{n_1, n_0\}$ and $t_i = \{t_1, t_0\}\ \forall\ i = \{\text{odd}, \text{even}\}$. Thus, the cladding consists of $N/2$ unit cells (pairs of layers) each with a total width $\Lambda = t_1 + t_0$ (the pitch). The odd layers have a higher index than the even layers such that $n_{\text{core}} \leq n_0 < n_1$.

Most of the theory discussed within is completely general. All numerical calculations, however, are based on a specific fibre structure and its equivalent 1-D cladding stack. This structure is based on the Bragg fibre of Temelkuran et al. [41]: the cladding layers were made from As_2Se_3 chalcogenide glass ($n \approx 2.8$) and the polymer polyethersulphone (PES, $n \approx 1.55$) with thicknesses of $270nm$ and $900nm$, respectively. A smaller core diameter (20 μm) than the cited fabricated fibre (≈ 700 μm), and fewer rings (4 pairs of layers instead of 9), are considered here due to numerical restrictions of the method employed (the relevant discretisations are stored in finite computer memory), but note that the bandgap behaviour would be very similar between the two structures regardless (like the 700 μm core, a 20 μm core also produces modes close to the n_{core}-light-line, demonstrated later in Fig. 3.7).

3.3 Background Theory

Here the theory used for the analyses of this chapter is presented. The reader should note that, as for Chapter 2, while attempts have been made to keep the treatment terse, it is still somewhat detailed and has the potential to break the flow of the discussion. If desired, one can skip directly to § 3.4 to delve directly into the results and discussion, since the text refers back to the relevant background material when required. Nonetheless, I have placed the following theory components into context as they are discussed to maintain the work's flow.

Save for the brief historical account of antiresonance models in § 3.3.1, Appendix A discusses all of the theory used in this Chapter. The relevant results are abstracted here for ease of reference. As discussed in the introduction, most of the content in Appendix A is not original to this Thesis, but has been re-derived and expressed in a consistent nomenclature for completeness and ease of discussion here. Those parts that are original are highlighted as such. The theoretical results derived in the body of this work are, to the best of my knowledge, original to this Thesis.

Section 3.3.1 provides a historical account of antiresonance models and how they relate to the SPARROW model developed within. Section 3.3.2 describes a ray-based modal analysis for both high- and low-index planar waveguides—critical to the definition of the SPARROW model. Section 3.3.3 then presents the pTMM formalism (discussed for the infinite layer case in § 2.3.2) for a *finite* number of layers; the evaluation of the reflectance of the composite system is discussed.

In addition to these methods, this Chapter also employs the infinite pTMM Bloch wave analysis (§ 2.3.2) and FEM technique (§ 2.3.4 and later in § 5.5).

3.3.1 Antiresonance—Historical Models

Originally discussed in the context of planar waveguides with a single high-index cladding layer by Duguay et al. in 1986 [173], the Anti-Resonant Reflecting Optical Waveguide (ARROW) model demonstrated how light could be confined to a low-index core by inhibited coupling (antiresonance) with a high-index cladding layer. The Duguay-ARROW model was later generalised to arbitrary numbers of cladding layers with arbitrary refractive indices by Archambault et al. [174] in 1993; the only restriction for core-guidance in the Archambault-ARROW model was that the core must have a refractive index equal to or less than the lowest of the cladding indices: $n_{\text{core}} \leq \min\{n_i\}$. By considering the transverse phase accumulated by a propagating ray (such as in § A.2.1.3) per round trip (*including* that from traversing the core, via the V-parameter) and equating it to 2π

(resonance), the Archambault-ARROW model determines the wavelengths at which the i^{th} cladding layer will be resonant with the light guided by the core [57, 174]:

$$\lambda_{m_i} = \frac{2t_i}{m_i}\sqrt{n_i^2 - n_{\text{core}}^2 + \left(\frac{U_\infty \lambda}{2\pi t_{\text{core}}}\right)^2}, \tag{3.1}$$

where $m_i \in \mathbb{Z}^+$ is the resonance order of the i^{th} layer type and U_∞ takes the value $(p+1)\pi/2$ for a planar core, with mode order $p \in \mathbb{Z}^+$, or value $j_{\nu\mu}$, with azimuthal and radial mode orders μ and ν respectively [such that the ν^{th}-order Bessel function satisfies $J_\nu(j_{\nu\mu}) = 0$], for a cylindrical core.

Note how in Eq. 3.1 the properties of the core are incorporated into the resonance conditions by default (via n_{core}, t_{core} and U_∞) such that the propagation constant of the core is built into the theory, thereby restricting it. In the SPARROW model defined within, the resonance analysis is completely decoupled from all core properties. Of critical importance is that the SPARROW model relates the cladding layer resonances to the core and core mode properties only via the effective mode index $\tilde{n}$. This allows consideration of *all* of the layers' full dispersion curves, when the layers are considered in isolation (Fig. 3.2). One can then infer a resonance effect in which the closer a core mode's $\tilde{n}$ lies to those of the isolated cladding layer modes, the stronger the resonance of the core light with the cladding, producing a larger core-mode confinement loss (CL). (This effect is actually demonstrated explicitly later via the FEM in § 3.6 and compared with the equivalent Bloch bandgap map.)

From the Archambault-ARROW model Eq. 3.1, the wavelengths producing antiresonance with individual cladding layers are found between the cladding layer resonance points by considering half-integer layer mode orders: $m_i \rightarrow m_i + \frac{1}{2}$ [174]. Using this simple approach, the Archambault-ARROW model has recently been applied successfully to depressed-core gas- and liquid-filled hollow-core integrated-ARROW waveguides [26, 57, 197] but tends to be used to optimise antiresonance with each cladding layer individually and only for the fundamental resonance ($m_i = 1$—*e.g.*, Ref. [57]). While this approach is sufficient for achieving a guidance regime, the tuning of each layer separately is unnecessarily restrictive (and potentially produces a higher confinement loss than desired by bringing the resonances of both layer types, rather than just one, close to the k of interest). As will be shown in § 3.7.2, a general analysis requires the resonances of all layer types to be considered together, leading to the definition of the *antiresonance mean point* $\overline{k}_c$ which enables a general antiresonance analysis for arbitrary cladding configurations and is strictly necessary for arbitrary $\tilde{n}$ and m_i (higher-order resonances/bandgaps below the low-index light-line).

By substituting $U_\infty \to \pi/2$ (planar core with $p = 0$) in Eq. 3.1, the Duguay-ARROW resonance condition [173] is derived where only one, high-index, cladding layer type is considered (making the i label redundant). This substitution is equivalent to assuming the core-bound rays only make glancing incidence with the cladding layer [173] and hence restrict the applicable regime to guided core modes close to the low-index light-line $\tilde{n} = n_0$. The Duguay-ARROW model has been successfully applied to different types of level-core ($n_{\text{core}} = n_0 < n_1$) ARROWs [173, 194, 195]. More recently, the Duguay-ARROW model has also been employed by Litchinitser et al.[99, 101, 102] and Abeeluck et al. [196] to describe antiresonance guidance in photonic crystal fibres (PCFs) in the large-core regime, including level-core Bragg fibres [99], and, in particular, PCFs with a cladding of high-index rods [101, 102]. For stratified claddings, the large-core limit reduces the cladding layer resonance condition to [99]:

$$\lambda_m = \frac{2t_1}{m}\sqrt{n_1^2 - n_0^2}. \tag{3.2}$$

Incidentally, note that $m \to m + \frac{1}{2}$ is required for the rod-cladding case, to accommodate for the modal cut-off frequencies of cylinders instead of planar layers [101, 102]. One important property of these level-core ($n_{\text{core}} = n_0$) waveguides is that the resonance effects of the cladding on the core-guided modes is dominated by the high-index inclusions, independent of the low-index region between them [99] (§ 1.2.3). This phenomenon is quantitatively explained (for layered claddings) in § 3.7.3 by setting $\tilde{n} = n_{\text{core}} = n_0$ in the SPARROW model.

3.3.2 Guidance in a Single Layer

The guidance of light within a single, isolated, layer (as represented in Fig. 3.2) is now considered. A detailed treatment is given in § A.2.1.3 in which both high-index layers in a low-index medium and low-index layers in a high-index medium are considered.

The basic principle is simple: waves propagating within a layer will be partially or totally reflected from the interfaces of the layer and bounding medium, trapping the reflected light within the layer. This is the fundamental premise of waveguidance, represented schematically in Fig. A.1.

Total internal reflection (§ A.2.1.2) is not considered here since, according to Corollary A.2, any ray originating from a low-index medium—which naturally requires $\tilde{n} \leq n_0$—cannot undergo total internal reflection within any surrounding parallel layer. This condition holds for the current work since the guidance region of interest has index $n_{\text{core}} \leq n_0$. Thus, only *leaky* guidance within a given layer is of interest here.

A layer waveguide will only support modes, leaky or otherwise, if the accumulated transverse phase for one round-trip of the slab (traversing the slab twice, reflecting from each interface) is an integer multiple of 2π (§ A.2.1.3). For both layers, the transverse phase accumulated by traversing the slab region once is $k_{\mathrm{i}x}t_{\mathrm{i}}$, Fig. 3.2. The forms of the low- and high-index slabs' phase relations thus differ only in their reflection terms.

Reflection of a ray with $\tilde{n} \leq n_0$ will accumulate a phase shift of 0 or π upon each reflection. Note that this implies the Goos-Hänchen phase shift is absent, which works in our favour here as its form is transcendental and thus cannot produce an analytic form. By having only these simple 0 or π phase shifts for any incidence angle, the final dispersion relations become fully analytic.

Equating the cumulative phase shifts to $m2\pi$ ($m \in \mathbb{Z}^+$), a unified mode dispersion relation for each waveguide can be derived [178, 198], Eq. A.99:

$$\tilde{n}_{m_i} = \left[n_i^2 - \left(\frac{m_i \pi}{t_i k} \right)^2 \right]^{\frac{1}{2}}, \quad m_i \in \mathbb{N}$$

where $i = 1$ corresponds to a high-index layer in a low-index background (Fig. 3.2 top-right) and $i = 0$ to a low-index layer in a high-index background (Fig. 3.2 bottom-right). Note how, just as for the tube structure earlier (§ 2.3.1), the $\tilde{n}$ of the guided modes is wholly independent of the cladding refractive index.

These analytic dispersion relations for the layers are critical to the general antiresonance model developed presently.

3.3.3 Finite Multilayer Stack

Section A.3.1 presents a planar transfer matrix method (pTMM) to describe the propagation of light through multilayer planar structures. By restricting the structure to two layer types, the method describes propagation through a finite Bragg stack, as in Fig. 3.2. Section 2.3.2 provided an overview of the treatment of § A.3.2 on the extension of this transfer matrix formulation to an infinite number of layers, permitting the existence of Bloch modes (the only eigen-solutions for an infinite periodic structure).

Only a finite number of layers is considered here. Instead of formulating a eigen-mode analysis[4] as for the infinite case, I consider the total reflectance of an incident wave on the full structure. In this case, the reflectance is essentially the cumulative effect of the reflection of each interface, taking the wave nature of the light into account (accounting for interference, hence resonance effects). This description is also more natural for describing the interaction of an incident (plane) wave upon the cladding structure as is desired here, instead of inference through calculating the behaviour of cladding modes (such as a Bloch-wave analysis), which I have not yet seen demonstrated in the literature (at least in the area of multilayer waveguides and antiresonance analyses—this approach does have a significant history in thin-film optics [199]).

Using the full system transfer matrix for a finite number (N) of layers, Eq. A.114:

$$M = \begin{pmatrix} M_{11} & M_{12} \\ M_{21} & M_{22} \end{pmatrix} = \left(\prod_{m=1}^{N} D_{m-1,m} P_m \right) D_{N,N+1}.$$

where the constituent interface and propagation matrices D and P account for the evolution of the fields across interfaces and through layers, respectively; they were described in § 2.3.2 above and in detail in § A.3.1.

Once M has been calculated, by relating the fields at the first and final interfaces, the total reflectance of the multilayer system can be evaluated as, Eq. A.117:

$$\mathcal{R} = |\Gamma_{0s}|^2 = \left| \frac{M_{21}}{M_{11}} \right|^2,$$

where Γ is the reflectance defined in § A.2.1.2 and M_{ij} is the element of M in the i^{th} row and j^{th} column. The 0 and s indices refer to the extreme outer (buffering) domains of the finite stack (§ A.3.1). $\mathcal{R}$ is thus ultimately a function of the light properties ($\tilde{n}$ and k) and the layer thicknesses (t_i) and refractive indices of all regions (n_i).

[4] which can be relatively easily done for the $\tilde{n} > n_0$ regime [36, 153].

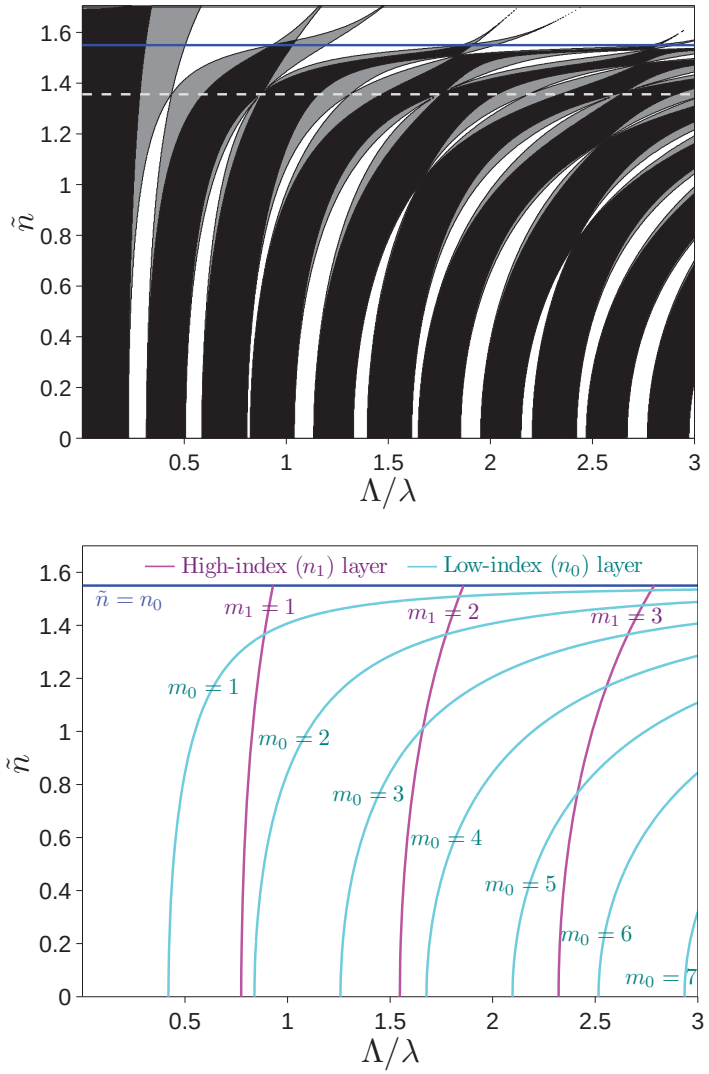

FIGURE 3.3: *Top*: A bandgap map generated via the Bloch theorem (§§ 2.3.2 and A.3.2) for a Bragg fibre cladding like that considered in Ref. [41]: $t_1 = 0.27$ μm, $t_0 = 0.9$ μm, $n_1 = 2.8$ and $n_0 = 1.55$. *Color scheme* (for $\tilde{n} < n_0$): as described in text, § 2.3.2; black for TE bands, black and grey for TM bands ($\Rightarrow$ white for TM bandgaps, white and grey for TE bandgaps). *Solid blue line*: the n_0-light-line. *Dashed line*: the Brewster line, $\tilde{n} = n_{\mathrm{B}}$. *Bottom*: A plot of all the SPARROW curves (dispersion curves of the equivalent isolated layers), via Eq. A.99, for the same cladding and bandgap domain. *Magenta*: high-index (n_1) layer, $\tilde{n}_{m_1}(k)$. *Cyan*: low-index (n_0) layer, $\tilde{n}_{m_0}(k)$.

3.4 The SPARROW Model

The Stratified Planar Anti-Resonant Reflecting Optical Waveguide model is a novel antiresonance model describing the resonance properties of arbitrary binary layered media, such as the claddings of depressed-core layered waveguides. It is a generalisation of the Archambault-ARROW model in that the core mode properties are decoupled from the cladding resonances, as described above. With the background theory developed, the formal definition of the SPARROW is rather straight-forward and is now discussed.

Formally, the model itself consists of the use of the resonance curves to describe various resonance, reflectance and bandgap phenomena. As discussed in §§ 3.3.2 and A.2.1.3, the resonance curves of a given layer (modal dispersion of the layers in isolation) are described by Eq. A.99:

$$\tilde{n}_{m_i} = \left[n_i^2 - \left(\frac{m_i \pi}{t_i k} \right)^2 \right]^{\frac{1}{2}}, \quad m_i \in \mathbb{N},$$

and correspond to a single pass transverse phase accumulation of $\phi = m_i \pi$ (the condition for resonance—constructive interference upon a round trip—within a layer). The characteristics of these curves and their relationships to each other (such as their intersection points or the regions they enclose) form the basis of the SPARROW model and will be discussed at length in the following sections. Note that $m_i = 0$, $\tilde{n} = 0$ and $k = 0$ are important special cases for the model, forming the limits within which it is applicable (discussed further later).

First, the phenomenological relationship between the bandgap of an infinite stack approximation to the cladding and the modal dispersion of the individual layers of the cladding considered in isolation will be considered. Figure 3.4 (top) is produced by overlaying the slab curves (Fig. 3.3—bottom) upon the corresponding Bragg stack's bandgap map (Fig. 3.3—top). A clear and striking similarity between the two plots is thus revealed: each high- and low-index slab dispersion curve corresponds to a band of the bandgap spectrum. Also, the gaps completely close at the intersection points of the high and low refractive index curves (n_{m_1} and n_{m_0}, discussed further in § 3.7.1). This is because $\tilde{n}_{m_1} = \tilde{n}_{m_0}$ implies optimal coupling between the two layer types so that light can easily propagate through the cladding, precluding the generation of a bandgap.

This is an example of how the resonance curves (and the properties derived from them—see § 3.7) can be used to quantitatively describe the resonant features of a layered structure (such as a waveguide cladding), including the properties of an associated bandgap spectrum. The SPARROW model thus gives direct physical insight into how the thicknesses and refractive indices of the constituent high- and low-index layers affect the

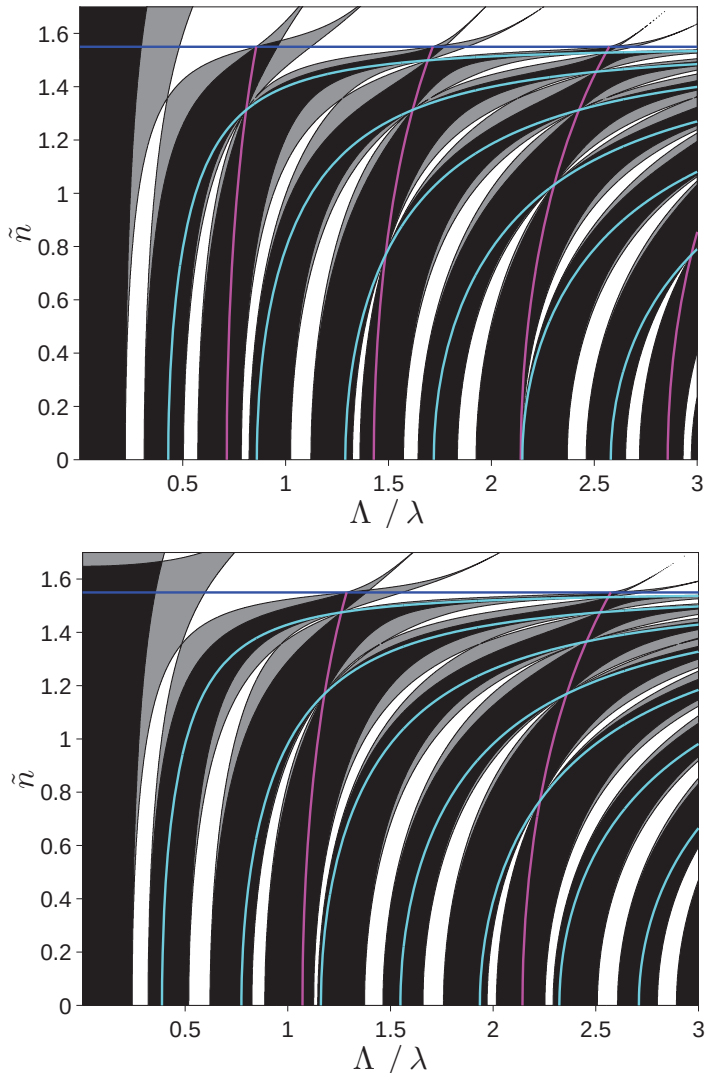

FIGURE 3.4: *Top*: The bandgap map of Fig. 3.3 with the cladding layer dispersion (SPARROW) curves (Fig. 3.3) overlayed. *Bottom*: The same configuration but with the high-index layer's thickness decreased: $t_1 = 0.27\ \mu$m $\rightarrow 0.18\ \mu$m. The bandgap topology dramatically changes between the two cases (new bandgaps are created). Using the nomenclature and analyses of § 3.7.5: $t_1 = 0.27\ \mu$m produces $N_1 = 2$ and $N_2 = 4$ whereas $t_1 = 0.18\ \mu$m produces $N_1 = 3$ and $N_2 = 6$.

resonant properties of the cladding. The model is thus similar to the Archambault-ARROW model [174] except that the latter inseparably couples the core properties to the resonance analysis. Instead, the SPARROW model considers the effective mode index alone, with no allusion to the properties of the core itself. In this way, the cladding resonances have been separated from the core properties, providing two benefits: the ability to easily describe cladding resonances on a bandgap-style $(\Lambda/\lambda, \tilde{n})$ plot (*e.g.*, Figs. 3.3, 3.4, 3.7 and 3.8); and the freedom to consider core modes of arbitrary $\tilde{n}$. The latter point requires that, for the SPARROW model to accurately predict core-mode spectral features, sensible values for a core mode's $\tilde{n}$ must be provided independently.

For large-core waveguides, this is trivial, since most low-order modes will lie very close to the n_{core}-light-line (demonstrated in § 3.6). However, it has also been shown that, at least for air-core Bragg fibres, it is possible to infer the (real part of the) core modes' $\tilde{n}$ solely from the core geometry [63, 147], including higher-order modes and small core ($\sim \lambda$) waveguides.

Note that between any two adjacent slab dispersion curves, a bandgap region exists in either the $\tilde{n}$ or k dimension, meaning that the discrete bandgaps within the stack bandgap spectrum are each *enclosed by a subset of the SPARROW curves*. The concept of a *bound region* for any particular bandgap is thus defined: the $(k, \tilde{n})$ region enclosed by the curves surrounding a particular bandgap. This behaviour implies the nontrivial discrete bandgap spectrum of the stratified cladding is replicated in position and topology by the equivalent SPARROW curves (including the physical limits $k = 0$, $\tilde{n} = 0$ and $\tilde{n} = n_0$, as discussed). Consequences and applications of this are discussed in § 3.7.

3.5 Reflectance, Resonances, and Bandgaps

It is clear that, at least phenomenologically (Fig. 3.4), there is a strong connection between the resonance/modal behaviour of both types of cladding layers considered in isolation and the Bloch wave bandgap spectra of the infinite Bragg stack built from them. A more fundamental approach to elucidating the connection between these phenomena is now considered.

First, the pTMM is used to derive analytic forms for the reflectance of each layer type, from which the conditions for minimising the reflectance is derived; it is shown how these conditions are identical to the resonances of the layers themselves (the SPARROW curves). The result constitutes an explicit analytic explanation of antiresonance for one (§ 3.5.1) and two (§ 3.5.2) layers. Only TE waves are considered here for simplicity; the only difference with the TM waves is that the Brewster effect dominates, producing $\mathcal{R} = 0$ about the Brewster condition $\tilde{n} = \tilde{n}_{\mathrm{B}} = n_i \sin(\theta_{\mathrm{B}})$ (§ A.2.1.2).

Second, in § 3.5.3, it is demonstrated how, by adding more and more layers to the system, the reflectance maps evolve into the Bloch-wave bandgap maps. This validates the assumption that light satisfying the Bloch-wave band conditions which is incident on an infinite stack will be transmitted through the stack, whereas light satisfying the bandgap conditions is reflected. More than this, it demonstrates how the light is either *totally* transmitted ($\mathcal{R} = 0$) or reflected ($\mathcal{R} = 1$) when within a band or bandgap, respectively; something which is best demonstrated using this direct reflectance approach, rather than inference from calculated cladding mode behaviour. Keep in mind that the reason why confinement loss of guided modes in a Bragg fibre, say, is non-zero (*e.g.*, Chapter 2) is, at least for the ideal case, related to the fact that realistic cladding structures must have a finite number of layers and hence non-unity reflectance (as demonstrated by all $\mathcal{R}$ maps in Figs. 3.5 and 3.6).

3.5.1 Relationships Between Reflectance and Antiresonance —Single Layers

By using the matrix method thoroughly described in § A.3.1, one can evaluate the transfer matrix for propagation onto and through a single layer embedded within an infinite homogeneous medium; namely those represented in Fig. 3.2 (right). The refractive index distribution of the system could thus be low-high-low or high-low-high.

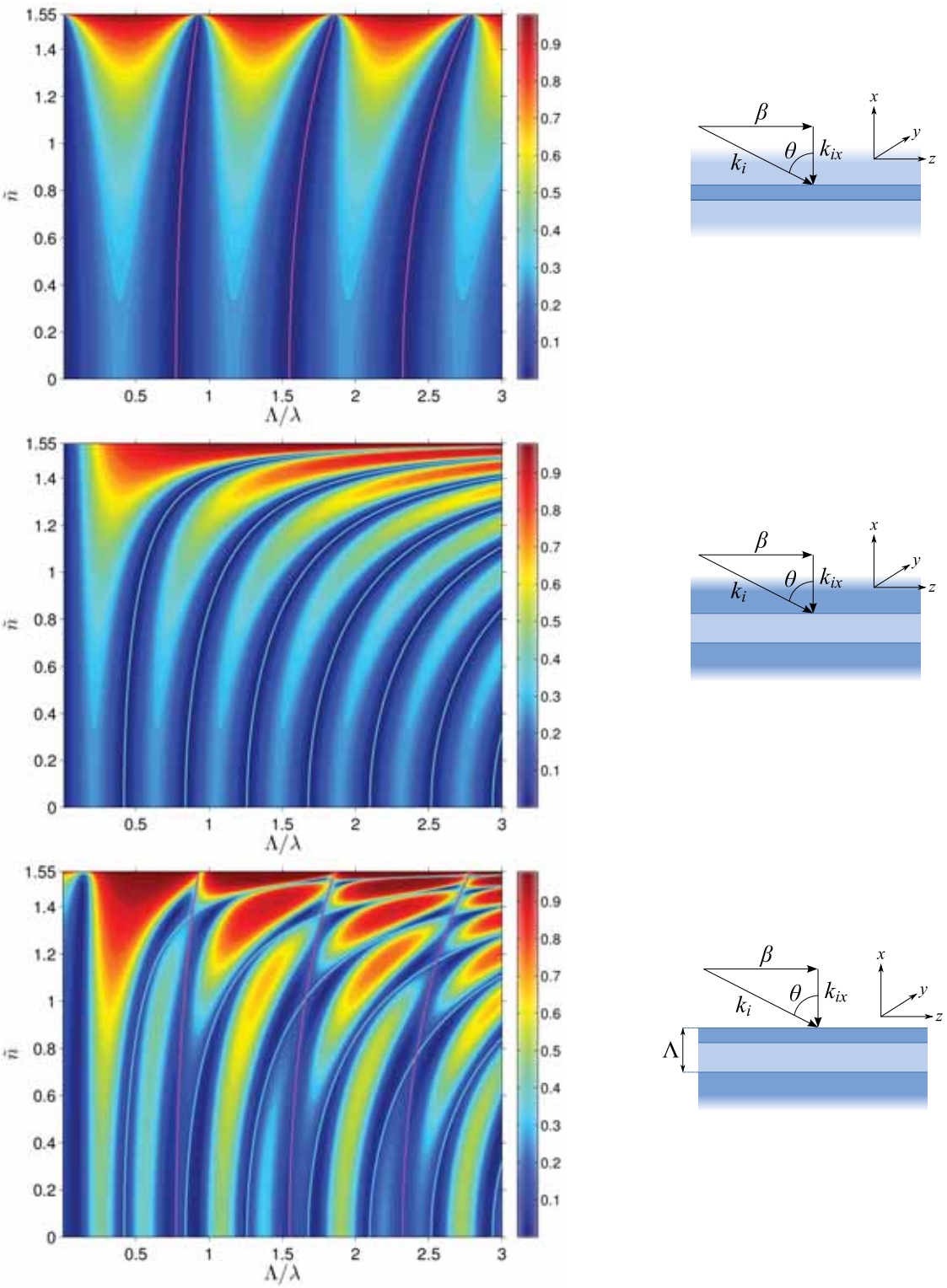

FIGURE 3.5: Reflectance maps $\mathcal{R}(\tilde{n}, \Lambda/\lambda)$ for TE polarised plane waves incident on isolated single high- and low-index layers and a two-layer planar stack based on the layer parameters (thicknesses and refractive indices) of the structure defined in § 3.2. *Top:* high-index layer in a low-index background (low-high-low). *Middle:* low-index layer in a high-index background (high-low-high). *Bottom:* 2-layer stack (low-high-low-high). the first two plots are overlayed with the mode trajectories of the supported modes in each layer. The 2-layer case is overlayed with the modes of the constituent layers considered in isolation; those of the first two single-layer cases. Qualitative representations of the planar structures for which the reflectances are calculated are shown to the right of the respective plot.

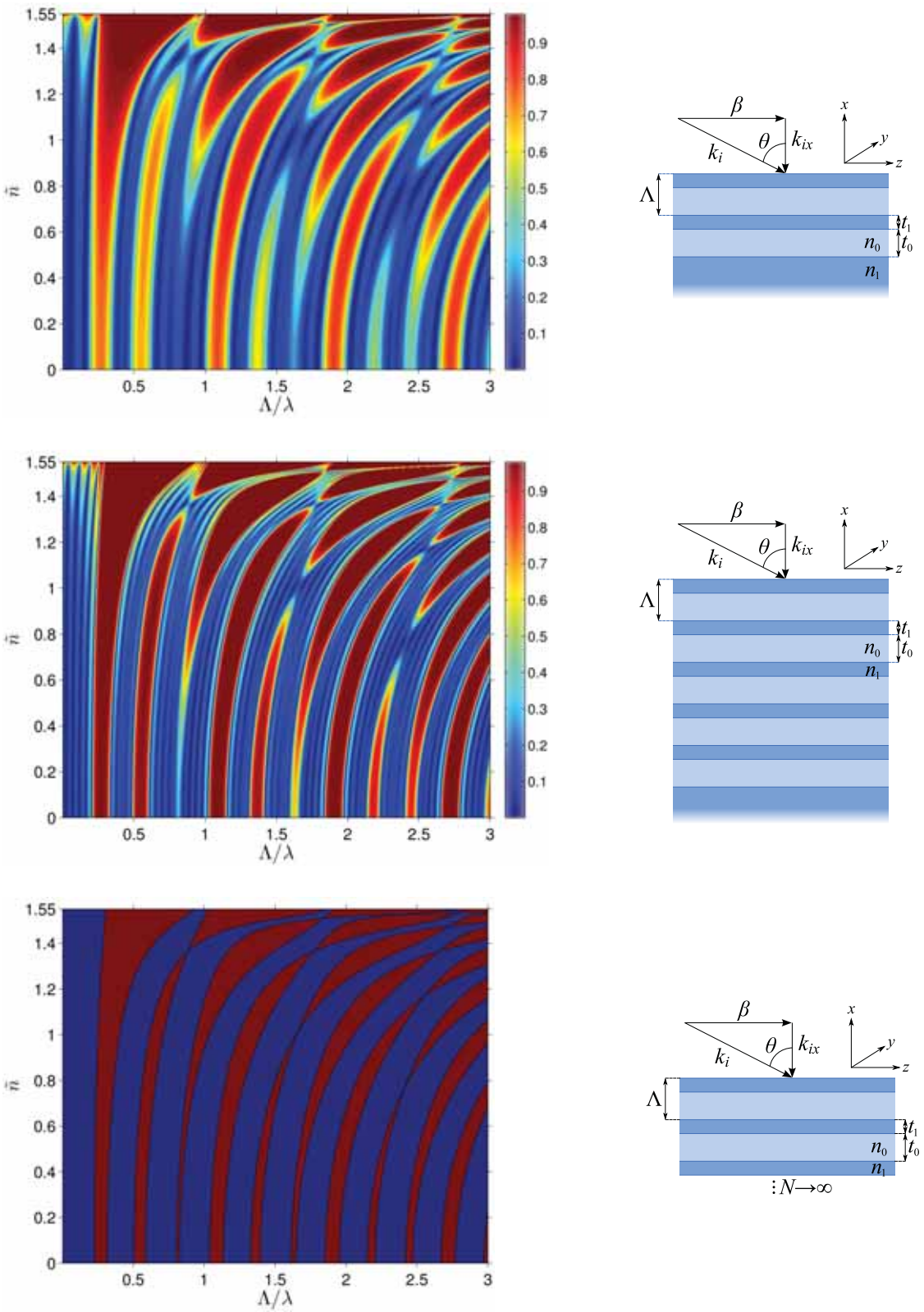

FIGURE 3.6: Reflectance maps $\mathcal{R}(\tilde{n}, \Lambda/\lambda)$ for TE polarised plane waves incident on multilayer planar stacks (*top:* 4-layer stack, *middle:* 10-layer stack) compared with the TE bandgap map of the infinite layer analogue (*bottom*—red regions represent the bandgaps and blue regions represent the allowed bands). This figure is an extension of Fig. 3.5.

For example, for the former, an incident wave first propagates through an infinite low-index medium and is then reflected from and transmitted through a high-index layer (two interfaces), the transmitted portion finally propagating into a second infinite homogeneous low-index medium (and similarly for the high-low-high case).

To generalise, let the layer have refractive index n_a and thickness t_a and the surrounding medium have refractive index n_b with infinite extent. From Eq. A.114, the transfer matrix relating the fields on one side of the layer to those on the other is:

$$\begin{aligned}
M =& D_\mathrm{ba} P_\mathrm{a} D_\mathrm{ab} \\
=& \frac{1}{T_\mathrm{ba} T_\mathrm{ab}} \begin{pmatrix} 1 & \Gamma_\mathrm{ba} \\ \Gamma_\mathrm{ba} & 1 \end{pmatrix} \begin{pmatrix} e^{i\phi_\mathrm{a}} & 0 \\ 0 & e^{-i\phi_\mathrm{a}} \end{pmatrix} \begin{pmatrix} 1 & \Gamma_\mathrm{ab} \\ \Gamma_\mathrm{ab} & 1 \end{pmatrix} \\
=& \frac{1}{T_\mathrm{ba} T_\mathrm{ab}} \begin{pmatrix} e^{i\phi_\mathrm{a}} + e^{-i\phi_\mathrm{a}} \Gamma_\mathrm{ba} \Gamma_\mathrm{ab} & e^{i\phi_\mathrm{a}} \Gamma_\mathrm{ab} + e^{-i\phi_\mathrm{a}} \Gamma_\mathrm{ba} \\ e^{i\phi_\mathrm{a}} \Gamma_\mathrm{ba} + e^{-i\phi_\mathrm{a}} \Gamma_\mathrm{ab} & e^{i\phi_\mathrm{a}} \Gamma_\mathrm{ab} \Gamma_\mathrm{ba} + e^{-i\phi_\mathrm{a}} \end{pmatrix} \\
\text{(by Eq. } A.83) \quad =& \frac{1}{T_\mathrm{ba} T_\mathrm{ab}} \begin{pmatrix} e^{i\phi_\mathrm{a}} - e^{-i\phi_\mathrm{a}} \Gamma_\mathrm{ab}^2 & (e^{i\phi_\mathrm{a}} - e^{-i\phi_\mathrm{a}}) \Gamma_\mathrm{ab} \\ -e^{i\phi_\mathrm{a}} - e^{-i\phi_\mathrm{a}} \Gamma_\mathrm{ab}^2 & e^{-i\phi_\mathrm{a}} - e^{i\phi_\mathrm{a}} \Gamma_\mathrm{ab}^2 \end{pmatrix} \\
=& \frac{1}{T_\mathrm{ba} T_\mathrm{ab}} \begin{pmatrix} e^{i\phi_\mathrm{a}} - e^{-i\phi_\mathrm{a}} \Gamma_\mathrm{ab}^2 & 2i \sin\phi_\mathrm{a} \Gamma_\mathrm{ab} \\ -2i \sin\phi_\mathrm{a} \Gamma_\mathrm{ab}^2 & e^{-i\phi_\mathrm{a}} - e^{i\phi_\mathrm{a}} \Gamma_\mathrm{ab}^2 \end{pmatrix}.
\end{aligned} \tag{3.3}$$

From Eq. A.117, the reflectance of an incident plane wave is thus:

$$\mathcal{R}_\mathrm{layer} = \left| \frac{M_{21}}{M_{11}} \right|^2 = \frac{|-2i \sin\phi_\mathrm{a} \Gamma_\mathrm{ab}^2|^2}{|e^{i\phi_\mathrm{a}} - e^{-i\phi_\mathrm{a}} \Gamma_\mathrm{ab}^2|^2}. \tag{3.4}$$

Since $\phi_\mathrm{a} \in \mathbb{R}$, implying $|e^{\pm i\phi_\mathrm{a}}| = 1$, the denominator can be evaluated as:

$$\begin{aligned}
|e^{i\phi_\mathrm{a}} - e^{-i\phi_\mathrm{a}} \Gamma_\mathrm{ab}^2|^2 =& \left| \frac{1 - e^{-2i\phi_\mathrm{a}} \Gamma_\mathrm{ab}^2}{e^{i\phi_\mathrm{a}}} \right|^2 \\
=& \left| 1 - \cos(2\phi_\mathrm{a}) \Gamma_\mathrm{ab}^2 + i \sin(2\phi_\mathrm{a}) \Gamma_\mathrm{ab}^2 \right|^2 \\
=& \left[1 - \cos(2\phi_\mathrm{a}) \Gamma_\mathrm{ab}^2 \right]^2 + \left[\sin(2\phi_\mathrm{a}) \Gamma_\mathrm{ab}^2 \right]^2 \\
>& 0 \quad \forall\, k,
\end{aligned}$$

where the final inequality holds since $\Gamma_\mathrm{ab} < 1$ here (no total reflection for $\tilde{n} \leq \min(n_\mathrm{a}, n_\mathrm{b})$, related to Corollary A.2), and Γ_ab has no explicit dependence on k. $\phi_\mathrm{a} = k_{\mathrm{a}x} t_\mathrm{a} = n_\mathrm{a} k \cos\theta_\mathrm{a}$ (§ A.3.1) obviously does have an explicit k dependence, though.

The numerator is directly evaluated as:

$$|-2i \sin\phi_\mathrm{a} \Gamma_\mathrm{ab}^2|^2 = 4 \Gamma_\mathrm{ab}^4 \sin^2\phi_\mathrm{a}.$$

The reflectance can then be expressed as:

$$\mathcal{R}_{\text{layer}} = \frac{4\Gamma_{\text{ab}}^4 \sin^2\phi_{\text{a}}}{\left[1-\cos(2\phi_{\text{a}})\Gamma_{\text{ab}}^2\right]^2 + \left[\sin(2\phi_{\text{a}})\Gamma_{\text{ab}}^2\right]^2}. \tag{3.5}$$

Therefore, since the denominator is always finite and non-zero for varying k, one finds that $\mathcal{R}_{\text{layer}} = 0$ when $\sin\phi_{\text{a}} = 0$ (ϕ_{a} having the only k dependence). This happens when $\phi_{\text{a}} = m\pi$, $m \in \mathbb{Z}$. This means the layer produces no reflection at all when $k_{\text{a}x} = m\pi/t_{\text{a}}$; all of the light is transmitted through the layer (by conservation of energy: $\mathcal{R} + \mathcal{T} = 1$, § A.2.1.2). Indeed, this is precisely the same condition required for *guidance* within the layer itself, as just discussed above in § 3.3.2, and discussed in detail in § A.2.1.3. This is, to the best of my knowledge, the first time such antiresonance effects have been analytically examined in this way.

Generalising somewhat, this behaviour is an explicit demonstration of what one could call the *resonance principle*:

> **Resonance Principle:** *Light incident upon a structural feature is minimally scattered from it when it satisfies the conditions for guidance within that feature;*

so that by extension, low-loss guidance is achieved when the guided light is antiresonant with the cladding features. While this phenomenon has been observed throughout the literature, such as that discussed in Chapter 1, to the best of my knowledge it has never been summarised in this general form[5]. While it may now seem trivial for structures such as the conventional level-core ARROW waveguide or ARROW fibre, this principle was not at all obviously applicable to arbitrary low-index guiding fibres and waveguides. This principle can be seen to extend well beyond just the planar case (hence cylindrical fibre case by extension) here, with recent literature furthering the connection between bandgap and antiresonance or tight-binding behaviour of many different types of structured fibres and waveguides with the modal properties of their individual cladding structural features [9, 130], as discussed in detail in Chapter 1.

Figure 3.5 explicitly demonstrates this important relationship between reflectance and guided modes; the contour maps represent $\mathcal{R}$ over a range of $\tilde{n}$ and $\Lambda/\lambda = \Lambda k/2\pi$ and the curves represent multiple orders of the dispersion function $\tilde{n}(k)$ of the layers' guided modes, all for the same structure as discussed in § 3.2. In this sense, $\tilde{n}$ and Λ/λ either completely describe an incident plane wave (essentially its incident angle and frequency)

[5] Although, I recall hearing a comment from Prof. Johnathan Knight in a a presentation of his [200] at the Conference for Lasers and Electro-Optics in 2009 of which I paraphrase: "It is becoming increasingly apparent to me that guidance within these types of waveguides (HC-MOF guidance) can be understood as interactions with a collection of waveguides that make up the cladding structure".

or the propagation constant of a guided mode satisfying the guidance criteria discussed above. The fact that $\tilde{n}$ and Λ/λ are unitless implies that the results of Figs. 3.5 apply for all globally scaled variants of the system (scaling the geometry and wavelength by the same factor), neglecting material dispersion.

On top of these reflectance maps are overlayed the $\tilde{n}(k)$ dispersion curves of the modes supported by the individual layers, discussed above in § 3.3.2 (represented in Fig. 3.3, bottom) and discussed in detail in § A.2.1.3. It is clear how the $\mathcal{R} = 0$ regions are perfectly mapped by the mode trajectories of the layers themselves, validating the above analysis and again explicitly demonstrating the resonance phenomenon. One can thus say that along the mode trajectories, the resonant behaviour produces the behaviour:

$$\mathcal{R}(\tilde{n}, k) = \mathcal{R}^{\text{res.}}_{\text{layer}} = 0 \quad \text{when} \quad \tilde{n}(k) = \sqrt{n_{\text{a}}^2 - \left(\frac{m\pi}{t_{\text{a}} k}\right)^2}. \tag{3.6}$$

This reflectance versus mode trajectory analysis is thus a novel way to not just describe but explicitly *explain* the waveguide resonance phenomenon.

Antiresonance can be similarly defined. Antiresonance is the opposite of resonance in that it produces a local maximum, not minimum, reflectance of light from a layer. Indeed, from Eq. 3.5 one can see that the denominator is minimised when $\phi_{\text{a}} = \frac{m\pi}{2}$. The numerator is maximised when $\phi_{\text{a}} = (m - \frac{1}{2})\pi$. In the k-dimension, then, $\mathcal{R}$ itself is thus maximised when $\phi_{\text{a}} = (m - \frac{1}{2})\pi$. In other words, reflectance is maximised when the mode condition $k_{\text{a}x} = (m - \frac{1}{2})\pi/t_{\text{a}}$ is satisfied. This condition defines dispersion curves that sit mid-way (in k) between the supported modes of the layer, due to the half-integer order. These half-order, anti-resonance, curves[6] thus represent the antiresonance condition in which $\mathcal{R}$ is maximised in k. More precisely, along such antiresonance curves, by enforcing $\phi_{\text{a}} = (m - \frac{1}{2})\pi$, this maximal reflectance has value:

$$\mathcal{R}(\tilde{n}, k) = \mathcal{R}^{\text{antires.}}_{\text{layer}} = \left[\frac{2\Gamma^2_{\text{ab}}}{1 + \Gamma^2_{\text{ab}}}\right]^2 \quad \text{when} \quad \tilde{n}(k) = \sqrt{n_{\text{a}}^2 - \left[\frac{(m - \frac{1}{2})\pi}{t_{\text{a}} k}\right]^2}. \tag{3.7}$$

which is independent of k as required. It is, however, dependent on $\tilde{n}$ (or equivalently, θ_{b}), *i.e.*, the maximum reflectance along the k-dimension between two adjacent layer mode curves depends explicitly on the value of $\tilde{n}$ (along the antiresonance curves). Since $\Gamma^2_{\text{a,b}} \to 1$ monotonically as $\tilde{n} \to n_0$ (or equivalently, as $\theta_{\text{b}} \to \pi/2$ for $n_{\text{b}} > n_{\text{a}} = n_0$ or $\theta_{\text{b}} \to \theta_{\text{c}}$ for $n_{\text{a}} > n_{\text{b}} = n_0$), demonstrated[7] by Fig. A.4, one can see this antiresonant reflectance value $\mathcal{R}^{\text{antires.}}_{\text{layer}}$ has physical limiting behaviour: finite at $\tilde{n} = 0$ (normal incidence) and as $\tilde{n} \to n_0$ (glancing incidence). In fact, the latter sees

[6] They aren't referred to as 'modes' since they don't correspond to the mode conditions; indeed, precisely the opposite.

[7] Since $\Gamma \in \mathbb{R}$ here, Γ^2 is identical to a reflectance.

$\mathcal{R}_{\text{layer}}^{\text{antires.}} \to 1$ monotonically as $\tilde{n} \to n_0$; as glancing incidence is approached, the light approaches complete reflection. This variation of reflectance with $\tilde{n}$ under antiresonance is quite different to reflection under resonance in which none of the light is reflected for all considered values of $\tilde{n}$: $\mathcal{R}_{\text{layer}}^{\text{res.}} = 0 \quad \forall\ \tilde{n} < n_0$. Finally, also note that, for a specific value of $\tilde{n}$, since Eq. 3.7 is independent of m, the maximum reflectance due to antiresonance has the *same value* regardless of the mode order of the resonances:

$$\mathcal{R}_{\text{layer}}^{\text{antires.}}\big|_{m,m+1} = \mathcal{R}_{\text{layer}}^{\text{antires.}}\big|_{m+1,m+2} \quad \forall\, m \in \mathbb{Z}^+. \tag{3.8}$$

This can be observed in the single layer reflectance plots in Fig. 3.5, where the local maxima clearly have the same value between resonances for any given $\tilde{n}$.

The special case of $\tilde{n} = n_0$ is essentially unphysical under this multilayer analysis: for $n_{\text{b}} > n_{\text{a}} = n_0$, the incident wave would have an incidence angle of $\pi/2$, unable to be reflected or transmitted across an interface at all; for $n_{\text{a}} > n_{\text{b}} = n_0$, the incident wave would have an angle of θ_{c} such that the transmitted wave would make an angle of $\pi/2$ with the normal, similarly unable to be reflected or transmitted across the second interface. Nonetheless, it is worthy to note that at $\tilde{n} = n_0$, $\mathcal{R}_{\text{layer}}^{\text{antires.}} = 1$, expected from the above limiting analysis, but[8] $\mathcal{R}_{\text{layer}}^{\text{res.}} = 1$, not 0, implying it has a singularity in this limit, as may be expected from such an unphysical case.

These results hold for *any* relative values of n_{a} and n_{b}, such as the top and middle images in Fig. 3.5. The antiresonance effect with high- *or* low-index layers is a critical and essential concept for much of this work.

This concludes the analysis of the reflectance of single isolated layers, but if one wishes to consider the behaviour of multilayer structures, the interference effects between adjacent high- and low-index layers must be considered as well as the aforementioned antiresonance effects of the individual layers themselves. For single layers, it was shown above that resonance can suppress reflection from a layer altogether. How do these resonance effects change when two layer types are put in close proximity in a multilayer structure, similar to the case of a Bragg stack? This is the question I now turn my attention to, providing a detailed analysis of the reflectance of a two-layer system and relating it to an antiresonance picture.

[8] Found by setting $\Gamma_{\text{ab}} = 1$ in Eq. 3.4.

3.5.2 Relationships Between Reflectance and Antiresonance —Two Layers

Figure 3.5 (bottom) shows a reflectance map similar to that for the single layers (top and middle) but for a two-layer case (low-high-low-high), *i.e.*, the reflectance of a plane wave incident from an infinite homogeneous low-index medium onto a high-index layer, then a low-index layer and then an infinite homogeneous high-index medium. The full transfer matrix for the system is the same as that of the infinite stack two-layer unit cell[9] in § 2.3.2 (§ A.3.2) $M = D_{01}P_1D_{10}P_0$ except that the low-index layer matrix component is followed by an interface matrix D_{01} to accommodate for propagation from a low-index (n_0) layer into an high-index (n_1) infinite homogeneous medium:

$$
\begin{aligned}
M &= D_{01}P_1D_{10}P_0D_{01} \\
&= \frac{1}{T_{01}^2T_{10}}\begin{pmatrix}1 & \Gamma_{01}\\ \Gamma_{01} & 1\end{pmatrix}\begin{pmatrix}e^{i\phi_1} & 0\\ 0 & e^{-i\phi_1}\end{pmatrix}\begin{pmatrix}1 & \Gamma_{10}\\ \Gamma_{10} & 1\end{pmatrix}\begin{pmatrix}e^{i\phi_0} & 0\\ 0 & e^{-i\phi_0}\end{pmatrix}\begin{pmatrix}1 & \Gamma_{01}\\ \Gamma_{01} & 1\end{pmatrix} \\
&= \frac{1}{T_{01}^2T_{10}}\begin{pmatrix}e^{i\phi_0}e^{i\phi_1}+e^{i\phi_0}e^{-i\phi_1}\Gamma_{01}\Gamma_{10} & e^{-i\phi_0}e^{-i\phi_1}\Gamma_{01}+e^{-i\phi_0}e^{i\phi_1}\Gamma_{10}\\ e^{i\phi_0}e^{i\phi_1}\Gamma_{01}+e^{i\phi_0}e^{-i\phi_1}\Gamma_{10} & e^{-i\phi_0}e^{-i\phi_1}+e^{-i\phi_0}e^{i\phi_1}\Gamma_{01}\Gamma_{10}\end{pmatrix}\begin{pmatrix}1 & \Gamma_{01}\\ \Gamma_{01} & 1\end{pmatrix} \\
&= \frac{1}{T_{01}^2T_{10}}\begin{pmatrix}e^{i(\phi_0+\phi_1)}+\Gamma_{01}^2\left[e^{-i(\phi_0+\phi_1)}-e^{i(\phi_0-\phi_1)}-e^{i(\phi_1-\phi_0)}\right] & \\ \qquad\Gamma_{01}\left[e^{i(\phi_0+\phi_1)}+e^{-i(\phi_0+\phi_1)}-e^{i(\phi_1-\phi_0)}\right]-\Gamma_{01}^3e^{i(\phi_0-\phi_1)} & \\ \Gamma_{01}\left[e^{-i(\phi_0+\phi_1)}+e^{i(\phi_0+\phi_1)}-e^{i(\phi_0-\phi_1)}\right]-\Gamma_{01}^3e^{i(\phi_1-\phi_0)} & \\ \qquad e^{-i(\phi_0+\phi_1)}+\Gamma_{01}^2\left[e^{i(\phi_0+\phi_1)}-e^{i(\phi_0-\phi_1)}-e^{i(\phi_1-\phi_0)}\right] & \end{pmatrix}
\end{aligned}
\tag{3.9}
$$

where the reciprocity relation $\Gamma_{ba} = -\Gamma_{ab}$ (Eq. A.83) has been used in the final line. The reflectance is evaluated from the first two matrix elements, as above $\mathcal{R} = |M_{12}/M_{11}|^2$.

From the figure, one can clearly see the influence of both the high- and low-index layer resonances; it appears as though the reflectance maps of the single layers have been multiplied together, with the maxima and minima of each dominating the topography creating discrete peaks in both the Λ/λ and $\tilde{n}$ dimensions. However, the multiplicative appearance is only approximate, with the exact $\mathcal{R}$ values also having contributions from interference effects between the two layers types. For example, the local maxima extend to lower $\tilde{n}$ compared to the single-layer cases; a result of constructive interference from reflections from the two layer types. The two-layer $\mathcal{R}$ map discretisation has a greater complexity than that seen in the single-layer maps (Fig. 3.5—top and middle) which each exhibited continuous bands which monotonically increased in maximum amplitude as $\tilde{n} = 0 \to \infty$. Note that the $\mathcal{R}$ minima no longer form continuous curves with $\mathcal{R} = 0$ because of these interference effects.

[9] Swapping the subscripts $1 \leftrightarrow 0$ in Eq. A.128

By overlaying the SPARROW curves [individual layers' $\tilde{n}(\Lambda/\lambda)$] upon the two-layer reflectance map (Fig. 3.5) one can see how the minima of the reflectance map are well approximated by the curves themselves. However, in contrast to the single-layer treatment above where the SPARROW curves agreed exactly with the reflectance minima, the curves here don't provide an exact agreement with the minima for the two-layer case. This can be appreciated from the fact that, as just discussed and shown in Fig. 3.5, the minima themselves don't form continuous bands, instead forming discrete local minima; such structural features are difficult to compare to a single curve even on face value. Naive expectations aside, one actually does find fascinating resonance behaviour hidden in the reflectance of the two layer system, as I now demonstrate.

The modes of the layer's considered in isolation (SPARROW curves), Eq. A.99, were solved for (§§ 3.3.2 and A.2.1.3) by asserting the accumulated phase for a guided wave (or more accurately, ray) was an integer multiple of 2π. The reflection components were shown to be equal to 0 or π because total reflection can not occur for $\tilde{n} \leq n_0$. The critical phase term was thus the phase shift induced by traversing the layer (Eq. A.98)[10]: $k_{ax}t_a = m\pi$. In the pTMM formulation used in the reflectance analysis here, this implies that resonance in the i^{th} layer type requires $\phi_i = m\pi$.

Resonance in the low-index layer thus requires $\phi_0 = m\pi$ which implies $e^{\pm i\phi_0} = (-1)^m$. Substituting this into M_{11} via Eq. 3.9 produces:

$$\begin{aligned} M_{11}|_{\phi_0=m\pi} &= (-1)^m \frac{e^{i\phi_1} - \Gamma_{01}^2 e^{i\phi_1}}{T_{01}^2 T_{10}} \\ &= \frac{(-1)^m e^{i\phi_1}}{T_{01}^2 T_{10}}(1 - \Gamma_{01}^2) \\ &= \frac{(-1)^m e^{i\phi_1}}{T_{01}^2 T_{10}}(1 + \Gamma_{01}\Gamma_{10}) \\ &= (-1)^m e^{i\phi_1}\frac{1}{T_{01}}, \end{aligned} \tag{3.10}$$

where the third and final steps follow from Eqs. A.83 and A.84, respectively.

For M_{12}:

$$\begin{aligned} M_{12}|_{\phi_0=m\pi} &= (-1)^m \frac{\Gamma_{01} e^{-i\phi_1} - \Gamma_{01}^3 e^{-i\phi_1}}{T_{01}^2 T_{10}} \\ &= \frac{(-1)^m \Gamma_{01} e^{-i\phi_1}}{T_{01}^2 T_{10}}(1 - \Gamma_{01}^2) \\ &= (-1)^m e^{-i\phi_1}\frac{\Gamma_{01}}{T_{01}}, \end{aligned} \tag{3.11}$$

where the final step follows from Eqs. A.83 and A.84.

[10] Up to an extra term of π to differentiate the low-index layer and high-index layer guidance/resonance.

One finds that the reflectance $\mathcal{R} = |M_{12}/M_{11}|^2$ (Eq. A.117) at resonance with the low-index layer is thus:

$$\mathcal{R}(\tilde{n}, k) = \Gamma_{01}^2 \quad \text{when} \quad \tilde{n}(k) = \sqrt{n_0^2 - \left(\frac{m\pi}{t_0 k}\right)^2}. \tag{3.12}$$

This is precisely the same expression (Eq. A.76) as for reflectance from a single low- to high-index interface!

Similarly, one can also evaluate the transmittance $\mathcal{T} = k_{sx}/k_{0x}|1/M_{11}|^2$ (Eq. A.118) where the indices 0 and s refer to the first and final homogeneous media, respectively. In the present case, $k_{sx} \to k_{1x}$ and k_{0x} remains the same (but the 0 index now refers to the refractive index n_0 instead of a label for the 'first' medium[11]). Using the form of Eq. 3.10, one finds:

$$\mathcal{T}(\tilde{n}, k) = \frac{k_{1x}}{k_{0x}} T_{01}^2 \quad \text{when} \quad \tilde{n}(k) = \sqrt{n_0^2 - \left(\frac{m\pi}{t_0 k}\right)^2}. \tag{3.13}$$

This is precisely the same expression (Eq. A.77) as for transmittance through a single low- to high-index interface. This could also have been inferred via the conservation of energy requirement $\mathcal{R} + \mathcal{T} = 1$ (§ A.2.1.2).

It is thus quantitatively true that, when light is resonant with the low-index layer, the reflectance and transmittance of the two-layer system is such that it is as if the layer is not present, *i.e.*, the light is reflected from or transmitted through the layer is of intensity as if the low-index layer's refractive index were increased to that of the high-index regions, creating an interface between two homogeneous low- and high-index regions. This has a direct parallel with the single-layer case above in which light resonant with a layer has a null reflectance from it, just as though it were not there.

The difference between the two-layer case to the single-layer one is the addition of an infinite homogeneous terminating region which creates a second layer against the first. By creating an extra interface in this way, instead of the reflectance, say, being null at resonance, it adopts a value dictated by the additional low- to high-index interface; just as though the low-index layer were absent in both cases.

In the same vein, resonance in the high-index layer thus requires $\phi_1 = m\pi$ which implies $e^{\pm i\phi_1} = (-1)^m$. Substituting this into M_{11} via Eq. 3.9, and noting the symmetry of the

[11] An unfortunate degeneracy in the nomenclature. Were the first medium to have had a refractive index n_1, say, then the label would have been altered as $k_{0x} \to k_{1x}$, where the 1 refers to the refractive index type.

exponential terms, produces:

$$\begin{aligned} M_{11}|_{\phi_1=m\pi} &= (-1)^m \frac{e^{i\phi_0} - \Gamma_{01}^2 e^{i\phi_0}}{T_{01}^2 T_{10}} \\ &= (-1)^m e^{i\phi_0} \frac{1}{T_{01}}, \end{aligned} \tag{3.14}$$

where the last step follows from Eq. 3.10.

For M_{12}:

$$\begin{aligned} M_{12}|_{\phi_1=m\pi} &= (-1)^m \frac{\Gamma_{01} e^{-i\phi_0} - \Gamma_{01}^3 e^{-i\phi_0}}{T_{01}^2 T_{10}} \\ &= (-1)^m e^{-i\phi_0} \frac{\Gamma_{01}}{T_{01}}, \end{aligned} \tag{3.15}$$

where the last step follows from Eq. 3.11. One can then evaluate the reflectance for resonance with the high-index layer as:

$$\mathcal{R}(\tilde{n}, k) = \Gamma_{01}^2 \quad \text{when} \quad \tilde{n}(k) = \sqrt{n_1^2 - \left(\frac{m\pi}{t_1 k}\right)^2}, \tag{3.16}$$

and the transmittance as:

$$\mathcal{T}(\tilde{n}, k) = \frac{k_{1x}}{k_{0x}} T_{01}^2 \quad \text{when} \quad \tilde{n}(k) = \sqrt{n_1^2 - \left(\frac{m\pi}{t_1 k}\right)^2}. \tag{3.17}$$

Just as for the low-index layer resonance above, these forms for the reflectance and transmittance are both as they would be for for a single interface. The explanation is also identical, except that in this case the high-index resonance makes it as if the high-index layer is not present, reducing the (power) response of the system to one in which the high-index layer is removed leaving behind a single low- to high-index interface.

Cursory inspection of the 2-layer reflectance map (Fig. 3.5) may suggest that the SPARROW curves don't correspond to the single-interface Fresnel reflectance values (Fig. A.4) since the curves are surrounded by peaks and troughs. Closer inspection, though, shows that the layer mode curves do correspond these single-interface values and represent a transition region between local peak and troughs in the two-layer $\mathcal{R}$ map due to constructive or destructive interference between the two layers as the light shifts off-resonance with one of the layers and hence begins to 'see' them both, rather than 'ignoring' one of the layers when resonant with it as just discussed. Because of this, the discrete regions defined by the SPARROW curves each contain a single large $\mathcal{R}$ maxima corresponding to constructive interference. This is an important point since, as more layers are added to the system, these maxima evolve into bandgaps. The evolution of finite reflectance maps into bandgap maps is discussed in the next section.

The last two sections have quantitatively demonstrated that for a single layer or two-layer (low-high-low-high) stack, when light is resonant with a layer, the reflectance and transmittance of the system is such that it is as if that layer is not present; a validation of the SPARROW model. I believe this analytic treatment to be unique and that it provides significant insight into the nature of the antiresonance mechanism by relating the reflectance of the structures considered directly and analytically to the supported modes of the constituent layers (the SPARROW curves). The consideration of both single high- or low-index layers and a two-layer stack demonstrates that this type of antiresonance effect and analysis holds not just for isolated layers but also for strongly coupled high- and low-index layers, the latter being a critical observation in order to apply it to multilayer stacks.

The extension of this analysis to cases of multiple high- and low-index layers ($N > 2$) sees the transfer matrices become increasingly complex and an analytic treatment is omitted here. Nonetheless, by numerically calculating the reflectance maps for increasing numbers of layers, shown in Fig. 3.6, the broad effects of the antiresonances can still be identified in that the resonances approximately correspond to the $\mathcal{R}$ minima. The evolution of the $\mathcal{R}$ maps to larger N is now discussed.

3.5.3 Evolution of Bandgaps for Multiple Layers

Figures 3.6 (top and middle) shows the reflectance maps for the same structure as Fig. 3.5 (bottom) but where the number of layers N has been increased to 4 then 10 from the original 2, respectively.

The most striking effect is the rapid convergence of all local R maxima toward a value of 1 and all minima toward 0. It was noted in the 2-layer analysis above that the local reflectance peaks increased in amplitude toward lower $\tilde{n}$ due to the greater number of interfaces capable of reflecting the light; when the reflected waves add coherently, the reflectance is larger than that of a stack with fewer layers because there are more layers capable of reflecting. For the 10-layer case one can see (Fig. 3.6—middle) that the cumulative coherent reflectance from all interfaces reflects almost *all* of the incident light within the high-reflectance bands and transmits almost all the light in the low-reflectance bands; the peaks thus form a table-top shape on the map surface (the dark red regions in Fig. 3.6, middle). The minima (dark blue regions) maintain their low value due to the resonant nature of the transmission as discussed above.

The edges of the bands appear 'blurred' such that the local table-top maxima have a smooth transition curve down to the valleys of the minima. The 2-layer case shown in Fig. 3.5 (bottom) demonstrates significant blurring of the edges, forming a relatively

slow gradation from the local maxima down to the minima. As more layers are added, as in Figs. 3.6 (top and middle), this gradual descent begins to become sharper, reducing the blurring of the band edges.

Also note that the minima valleys contain many thin local ridges with lower value than the extended maxima bands and can be seen in Figs. 3.6 (top and middle). For the case of multiple ridges, they increase in maximum amplitude toward the edges of the main bands, as in Figs. 3.6 (middle). These ridges are due to higher-order interference between the unit cells of the stack; there are typically $N/2-1$ ridges between the maxima bands. The 2-layer structure of Fig. 3.5 (bottom) does not exhibit any ridges because it only has a single unit cell. In each case, there also appears to be an extra ridge along the $k = 0$ ($\Lambda/\lambda = 0$) axis. The nature of these higher-order interference ridges, while interesting, is not so important here. What is important is to note how their amplitude tends to decrease as they become more numerous with the addition of extra layers, gradually flattening the amplitude of the (dark blue) minima valleys towards $\mathcal{R} = 0$.

So, as more layers are added to a stack, the local maxima peaks increase towards $\mathcal{R} = 1$ and flatten out to a table-top while the minima valleys decrease and flatten out to $\mathcal{R} = 0$. Importantly, the edges distinguishing the band of peaks from the valleys becomes sharper, forming distinct banded domains. In fact, one can see that the distribution of the reflectance map is approaching that of the Bloch-wave band diagram for an infinite-layer equivalent stack, shown in Fig. 3.6 (bottom)—only the TE bands are shown since the reflectance calculations above considered only the TE polarisation. The colour scheme for the Bloch bands and bandgaps is matched here to that of the maximum and minimum reflectance values, respectively, shown in Figs. 3.5 and 3.6. The bandgap map itself is otherwise identical to that is Figs. 3.3 (top) and 3.4 (top).

The evolution of the structure of the reflectance maps toward that of the Bloch-wave band maps can be explained by similar observations as given in § 2 for the confinement of core modes of a Bragg fibre to the cladding bandgaps: light incident upon the stack is subject to the same boundary conditions and interface impedance as that of modes that would be supported in the stack. This was observed analytically for the more simple case of single- and two-layer stacks in terms of resonances with the layers themselves. The critical difference for multiple layers is that the more complex structure can support a larger number of modes owing to the interactions of the all layers in the stack. An infinite number of layers supports a continuum of Bloch modes within the allowed bands (dark red regions of Fig. 3.6, bottom) and no modes in the bandgaps (dark blue regions). For many layers, then, just as for the supported Bloch modes, incident light satisfying the allowed Bloch band conditions will be preferentially supported by the structure and allowed to pass through it, just as light satisfying the mode condition of a single layer is

allowed to be totally transmitted through it (§ 3.5.1); similarly, incident light satisfying the bandgap conditions will not be supported by the structure and hence reflected, again similar to the single-layer case above.

There are also parallels here with the photonic tight-binding model discussed in § 1 in that the Bloch modes residing predominantly in a specific feature/layer define the band edges. The implication here is that, due to the evident evolution of the reflectance maps towards the structure and topology of the bandgap maps, the PTBM also defined the sharp transitions of the reflectance map for high-N multi-layer stacks, *i.e.*, in the same way as I have shown here that the sub-light-line antiresonance conditions (SPARROW curves) define (for single layers) or approximate (for multiple layers) the $\mathcal{R}$ minima for the 'blurred' low-N reflectance maps, the PTBM thus defines the sharp transition regions $\mathcal{R} = 1 \rightarrow 0$ shown by high-N multi-layer stacks.

This also validates the assumption that light satisfying the Bloch-wave band conditions which is incident on an infinite stack will be transmitted through the stack, whereas light satisfying the bandgap conditions is reflected (as argued in the core-mode analysis of § 2). More than this, it also demonstrates how the light is either totally transmitted of reflected when within a band or bandgap, respectively; something which is best demonstrated using this direct reflectance approach.

Note that as the band edges of the reflectance maps become sharper and better defined with the addition of extra layers to the structure, the saddle-points corresponding to the intersection of the SPARROW curves begin to become sharper, tending towards a singularity. This explains why the Bloch mode bands close to a point at the SPARROW curve intersections.

3.5.4 Summary

In summary, §§ 3.5.1 and 3.5.2 imply:

- The resonances of a single isolated high- or low-index layer exactly determine the conditions of no reflectance from that layer, *i.e.*, layer modes $\tilde{n}_{m_i}$ correspond to $\mathcal{R} = 0$, allowing all light to pass through the layer. The maximum reflection from the layer corresponds to half-order resonances $m_i - 1/2$—antiresonance.
- The same resonances for a 2-layer stack (low-high-low-high) reduce the reflectivity of the structure to that of a single interface. As for the single-layer case, resonances with a certain layer type make the system respond (with respect to reflected and transmitted power) as if that layer were absent from the structure. The reflectance minima exist close to the resonances (the mode trajectories of the

layers in isolation). Antiresonances reside in the bound regions of all resonance curves—analysed further below.

- The 'blurred' reflectivity map of the 2-layer structure evolves into the sharp-edged Bloch band map structure as more layers are added to the stack. The reflectance maxima $\mathcal{R} = 1$ regions correspond to the Bloch wave allowed bands whereas the reflectance minima $\mathcal{R} = 0$ regions correspond to the Bloch wave bandgaps. This provides a consistent picture of reflectance vs. supported modes as for the more simple single- and 2-layer cases. Due to the robust evolution toward the bandgap structure, the equivalence of the SPARROW curve topology with that of the bandgap map as observed above (§ 3.4) is explained.
- For all cases one deduces: if guidance of light is supported in a structure, it is efficiently transmitted through the structure when externally incident; if guidance of light is not supported in the structure, it is reflected. This is the Resonance Principle as defined above and is responsible for the antiresonance phenomena discussed in the literature reviewed in Chapter 1 and throughout this Thesis.

Section 3.5.3 implies:

- Few layers produce reflection from a layered medium (such as a depressed-core waveguide cladding) in a manner closest to an antiresonance regime, whereas many layers produce reflection behaviour closer to a bandgap regime. Numerical demonstration given with discussion of the underlying physical mechanisms. One can thus conclude that the SPARROW model will best describe high-loss regions of depressed-core multilayer waveguides for a small number of layers, whereas the Bloch wave analysis is better suited for many layers (as the Bloch band edges become more well-defined, due to the increasing number of modes within the multilayer stack converging to the continuum of Bloch modes). Because of this relationship between the two regimes, the it is found that the SPARROW model can be used as an analytic tool to describe many features of the associated bandgap spectrum, as will be shown in the following sections.
- An explicit verification of arguments presented in Chapter 2 in that modes (incident plane waves here) with effective mode indices close to the low-index light line ($\tilde{n} \approx n_0$) produce the lowest confinement loss since the cladding reflects light most efficiently in that regime. The reflectance maps above demonstrate this effect directly, clearly revealing the trend that the maximum reflectance within a given bound region increases the closer it is to $\tilde{n} \approx n_0$; the extreme case being the regions terminating on $\tilde{n} = n_0$ which, as discussed, produce a maximal reflectance of unity.

3.6 Confirmation via FEM Analysis

The validity of the SPARROW model for determining the low-loss guidance spectral regions of binary layered-cladding waveguides for $1 \leq \tilde{n} \leq n_0$ is verified directly here by calculating the confinement loss spectrum of a particular Bragg fibre configuration in which both high- *and* low-index resonances are evident. For this, the realistic depressed-core Bragg fibre parameters of Ref. [41] discussed in § 3.2 are considered, with a few alterations.

First, the core refractive index is altered to be $n_{\text{core}} = 1.45$ rather than 1 (air/vacuum) since this index value produces core modes with effective mode indices in about the middle of the bandgap spectrum in the $\tilde{n}$-dimension. This could be achieved experimentally by filling the hollow core with a liquid of refractive index 1.45—achievable with index-matching liquids or various oils; Chapter 4 demonstrates this experimentally by systematically filling the core of a Bragg fibre with a range of liquids of various refractive indices. Intercepting the bandgap structure within the region $1 \leq \tilde{n} \leq n_0$ (accessible only by depressed-core configurations such as a liquid-filled Bragg fibre) reveals nontrivial and interesting spectral structure; it provides an ideal scenario in which to demonstrate how the resonances described by the SPARROW model can anticipate the large confinement loss regions of the core modes guided within these cladding bandgap regions.

Second, the parameters of the extended structure are relaxed. A smaller core diameter of 20 μm is considered rather than the that of the cited fabricated fibre's ≈ 700 μm [41]. Fewer rings are also considered: 4 pairs of layers instead of 9 [41]. These parameters result in a smaller structure to model numerically, working within the numerical restrictions imposed by the calculation method employed (FEM); the relevant discretisations are stored in finite computer memory—the smaller the structure, the lower the required memory. These alterations will not significantly affect the observed bandgap and antiresonance behaviour calculated; like the 700 μm core, a 20 μm core also produces modes close to the n_{core}-light-line, Fig. 3.7, thus intercepting the bandgap spectrum at approximately the same positions.

A finite element method is used to model the modal behaviour of the waveguide via the commercial FEM package COMSOL Multiphysics. Perfectly matched layers (PMLs) [182] are employed in order to solve for the complex $\tilde{n}$, and hence for the confinement loss $\text{CL} = 20\log_{10}(e)k\text{Im}\{\tilde{n}\}$ (Eq. A.25). The FEM method and PMLs were discussed in § 2.3.4.

Figure 3.7 shows the TE_{01} core mode dispersion trajectory $\tilde{n}(\Lambda/\lambda)$ and confinement loss $CL(\Lambda/\lambda)$ spectra for the considered fibre structure. The mode trajectories are overlayed

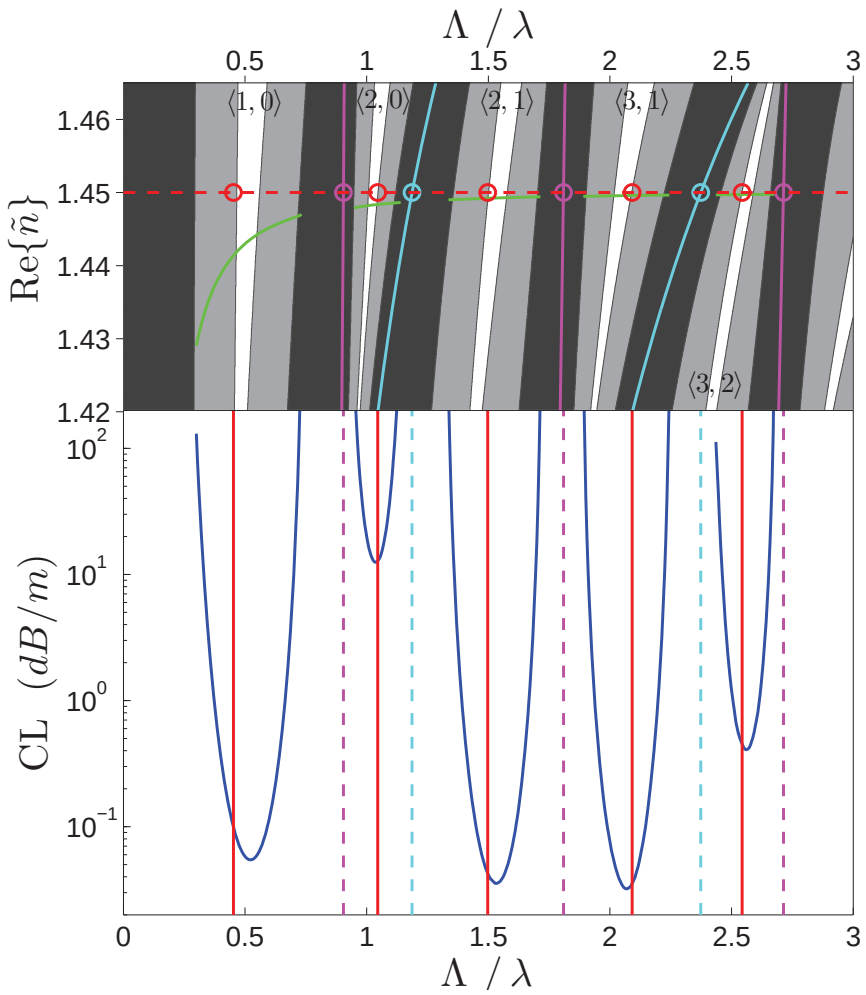

FIGURE 3.7: **Top**: A portion of the SPARROW curves and bandgap map from Fig. 3.3. *Green line*: the TE_{01} mode's $\mathrm{Re}\{\tilde{n}\}$ from the FEM calculation of the equivalent Bragg fibre, with a core of size $t_{\mathrm{core}} = 20\ \mu$m. *Red dashed line*: the n_{core}-light-line ($\tilde{n} = 1.45$). *Red circles*: positions of the antiresonance mean point $\overline{k}_c$ (§ 3.7.2) on the n_{core}-light-line. The gaps are labelled using the nomenclature of § 3.7.1. The limit value $\Lambda/\lambda = 3$ corresponds to $\lambda = 390nm$ in this case. **Bottom**: The associated CL spectrum (*blue curves*). *Cyan and magenta dashed lines*: low- and high-index SPARROW resonances on the n_{core}-light-line, respectively (corresponding to circles of the same color in the top plot). *Red lines*: positions of the antiresonance mean points from the top plot (red circles).

upon the analogous infinite 1-D stack cladding bandgap map. Since only the TE_{01} mode is considered here (for similar reasons as discussed in Chapter 2 for considering low-order modes), only the TE Bloch bands (black regions) will have influence over the guided core modes; the TM bands (black and grey regions) are shown for completeness. The bandgap region shown is a portion of the same band map as shown in Fig. 3.3. The mode trajectories of the equivalent isolated cladding layers (the SPARROW curves) are overlayed upon the band map.

Note how the Bloch bands are again approximated by the SPARROW curves (magenta

and cyan lines) in their location on the $(\tilde{n}, \Lambda/\lambda)$ plane. This is as already demonstrated in § 3.4 (*e.g.*, Fig. 3.4) and explained in § 3.5; Fig. 3.7 is just a zoomed-in version of Fig. 3.4 (top). This waveguide structure and section of the band map ($\tilde{n} \approx n_{\text{core}} = 1.45$) is particularly interesting because the higher-order bands correspond to both high- *and* low-index SPARROW curves. This means the modes bound to the core of the Bragg fibre will be influenced by resonances of both layer types. This is a generalisation of the behaviour of level-core waveguides which are dominated by resonances of only high-index features in accordance with the ARROW model, as discussed in Chapter 1. In fact, in § 3.7.3, this level-core resonance behaviour is analytically shown to be a special case of the more general depressed-core behaviour shown here.

As expected from the discussions of § 2, Fig. 3.7 also shows how the supported TE_{01} mode exists only within the cladding bandgaps. In accordance with the bandgap guidance mechanism, no mode solutions exist within the allowed bands (light is permitted to propagate through the cladding). From the reflectance picture above (§ 3.5) the non-existence of core mode solutions arises from the low-reflectance of the cladding which approximately correspond to the Bloch wave band maps: reflectance minima (maximum transmittance) of light incident upon the cladding approximately corresponds to cladding bandgap regions; light in these regions is efficiently transmitted through the cladding, extinguishing the supported core modes.

The most important observation here is that the CL spectrum of Fig. 3.7 (bottom) shows how the core-mode loss dramatically increases as the Bragg fibre core modes approach the SPARROW resonance features. Here the resonances are the isolated layer mode trajectories evaluated on the $\tilde{n}_{\text{core}}$-light-line ($k_{m_i}(n_{\text{core}})$ via Eq. A.100). The light-line intersections withe the SPARROW curves is a good approximation to the core mode resonances here since, as shown in Fig. 3.7, the considered mode lies close to the core's light-line $\tilde{n} \approx n_{\text{core}} = 1.45$ (expected from large-core waveguides as discussed). This example clearly demonstrates how the SPARROW model truly is a generalised antiresonance model for guidance below the low-index light line $\tilde{n} \leq n_0$. It is also apparent that the resonant properties of both high- and low-index layers must be considered when evaluating the resonances for arbitrary $\tilde{n}$. The separation of the cladding layer resonances from the core mode behaviour is what sets the SPARROW model apart from the Archambault-ARROW model and the results shown here highlight just how important this separation is in the analysis of depressed-core layered waveguides. Owing to this separability and the importance of the resonances of both layer types, the interactions and relationships between the SPARROW curves is analysed in detail in the following sections.

One example of the importance of considering both layer type resonances is seen in that the minimum CL for each gap falls close to mid-way (in frequency) between the adjacent cladding resonance points. This critical point is discussed further in § 3.7.2 and is vital for the antiresonance predictive component of the SPARROW model, permitting the definition of an antiresonance condition in the presence of not one but two dominant layer type resonances. Incidentally, the CL spectra of the next two higher-loss modes, TM_{01} and HE_{11}, have values above the domain presented in Fig. 3.7 (bottom), unsurprisingly (due to the narrow TM bandgap due to the Brewster effect, Fig. 3.3) and is commensurate with the predicted effectively-single-mode behaviour of Bragg fibres [63, 171].

As for the level-core case in Chapter 2, and the cited cases discussed in Chapter 1, one sees that the antiresonance curves only provide an approximation to the limits of the low-loss regions of the core mode: the CL curves rise rapidly closer to the bandgap edges than the resonance points—with the latter proving a good approximation. For the level-core cases it was argued that the interactions between the dominant high-index features of the cladding were responsible for broadening the resonances into continuous bands. In the depresses-core case here, it is difficult to make an analogy with this explanation since both the high- and low-index layers are dominant. In the level-core case, the low-index regions served only to separate the high-index features; the larger the low-index regions, the weaker the interactions between the high-index features and hence the more narrow the bands surrounding the resonances. Here, the thickness of the low-index layers has a direct influence on the loss spectrum: the larger the low-index regions, the more modes are supported in the low-index layers. The increased mode volume would produce more low-index resonances to interrupt the core mode trajectory. In other words, once again one must appreciate that, in the depressed-core regime, the influence of both layer types is critical, highlighting the importance of the SPARROW model. The non-zero width of the Bloch bands for $\tilde{n} < n_0$ thus can't be explained by the large t_0 limiting argument used for the level-core regime; the sub-n_0-light-line Bloch bands must be considered as a result of the interaction of all layers (high- and low-index alike) in the generation of a continuum of Bloch modes. The SPARROW resonances only approximate those Bloch modes that may reside predominantly in one or the other layer type, similar to the photonic tight-binding models discussed in Chapter 1 (but differing in that isolated layer modes, not infinite stack Bloch modes, are considered, as required of an antiresonance model).

These observations also explain why the higher-order gaps of this $\tilde{n} < n_0$ case do not necessarily support modes of lower confinement loss compared to their lower-order counterparts; this behaviour is in contrast to the $\tilde{n} \approx n_0$ case discussed in Chapter 2 where gaps close to the n_0–light-line were shown to produce modes of lower minimum CL for

increasing gap order. In the depressed-core regime considered here, the low-index resonances must be considered: their introduction of nontrivial gap closure points with the high-index resonances produces a much more complicated bandgap spectrum than that of the level-core case. The core modes thus intercept the nontrivial gap spectrum at points where the width of adjacent gaps differs considerably from one to the next, unlike the level-core case in which all gaps along the n_0–light-line have a similar width (with respect to ω or k). Thus, since the CL increases as the bandgap edges are approached [63, 64], a variety of gap widths will produce a variety of minimum CL values attainable within the intercepted bandgaps, as seen in Fig. 3.7. In short: core modes in the $\tilde{n} < n_0$ regime intercept a more complex bandgap spectrum than those in the $\tilde{n} \approx n_0$ regime, producing a greater variety of minimum CL values attainable in the higher-order gaps along the core mode trajectory.

3.7 Further Analysis of the SPARROW Model

Here the relationships between the SPARROW curves are analysed. This is where the analyticity of the model becomes most useful. Many nontrivial properties of the cladding resonances, and hence of the associated bandgap spectra, are derived in wholly analytic forms.

By deriving the following properties and relationships in this manner, the antiresonance picture of light guidance in depressed-core Bragg waveguides is 'solved' in the sense that one can use relatively simple expressions to evaluate many nontrivial properties of the resonant response of a given waveguide structure. Evaluation of all expressions below typically only require the knowledge of the core-guided modes' $\tilde{n}$, the cladding layer refractive indices n_i, the layer thicknesses t_i, the order of the layer resonances of interest m_i, and the wavelength of interest λ.

Expressions relating the antiresonance and bandgap pictures will be derived for the following properties:

- the intersection points of any two SPARROW curves and hence the precise closure points of any given gap (§ 3.7.1),
- a consistent nomenclature for arbitrary SPARROW or bandgap spectra (§ 3.7.1),
- the approximate position of lowest core-mode confinement loss within any bound region or gap, defining a generalised antiresonance condition (§ 3.7.2),
- the antiresonance-based 'center' of a bound region and, by inference, of a bandgap, in both $\tilde{n}$- and k-dimensions (§ 3.7.4),
- and the number of bound regions (hence bandgaps) within a specific domain, thus the associated bandgap spectrum topology (§ 3.7.5).

In doing so, it is further demonstrated (in addition to the discussions above) how there exists an intimate relationship between the bandgap and antiresonance pictures of light confinement in binary-layered-cladding waveguides on and *below* the low-cladding-index light-line. This implies that Bragg fibres and integrated-ARROWs, say, guide by fundamentally the same principles even though each are typically ascribed to a bandgap or anti-resonance guidance mechanism in the current literature, as discussed above.

3.7.1 Curve Intersections and Gap Nomenclature

As has been demonstrated, the bandgaps of an infinite Bragg stack close upon the points at which two high- and low-index layer dispersion curves meet. Clearly, an analytic expression, if it exists, for the locations of these points is desirable, if only for reasons of

ease of calculation, physical insight and completeness. Indeed, such an analytic expression for arbitrary intersection points will be derived here. As will be shown in § 3.7.5, one example of the application of such expressions for the SPARROW intersections (hence gap closure points) is that they can be used to express the topology of an arbitrary bandgap spectrum (in this case, how many gaps exist within a given sub-domain).

The intersection points of the high- and low-index layer dispersion curves can be found by equating either $\tilde{n}(k)$ or $k(\tilde{n})$ for a pair of modes with indices m_1 and $m_0 \in \mathbb{N}$.

First consider two arbitrary high- and low-index dispersion curves $\tilde{n}_{m_1}(k)$ and $\tilde{n}_{m_0}(k)$, respectively. By equating their functional forms as given by Eq. A.99:

$$\begin{aligned}
\left[n_1^2 - \left(\frac{m_1\pi}{t_1 k}\right)^2\right]^{\frac{1}{2}} &= \left[n_0^2 - \left(\frac{m_0\pi}{t_0 k}\right)^2\right]^{\frac{1}{2}} \\
\Rightarrow \qquad n_1^2 - n_0^2 &= \left(\frac{m_1\pi}{t_1 k}\right)^2 - \left(\frac{m_0\pi}{t_0 k}\right)^2 \\
&= \frac{\pi^2}{k^2}\left(\frac{m_1^2}{t_1^2} - \frac{m_0^2}{t_0^2}\right) \\
\Rightarrow \qquad k^2 &= \frac{\pi^2}{n_1^2 - n_0^2}\left(\frac{m_1^2}{t_1^2} - \frac{m_0^2}{t_0^2}\right)
\end{aligned}$$

Implying that the k-coordinate of the intersection point is:

$$k = \left[\frac{\pi^2}{n_1^2 - n_0^2}\left(\frac{m_1^2}{t_1^2} - \frac{m_0^2}{t_0^2}\right)\right]^{\frac{1}{2}} \tag{3.18}$$

Similarly, by equating the functional forms for the inverse functions $k(\tilde{n})$ of the same curves as given by Eq. A.100:

$$\begin{aligned}
\frac{m_1\pi}{t_1}\left[n_1^2 - \tilde{n}^2\right]^{-\frac{1}{2}} &= \frac{m_0\pi}{t_0}\left[n_0^2 - \tilde{n}^2\right]^{-\frac{1}{2}} \\
\Rightarrow \qquad n_1^2 - \tilde{n}^2 &= (n_0^2 - \tilde{n}^2)\left(\frac{m_1 t_0}{m_0 t_1}\right)^2 \\
\Rightarrow \qquad \tilde{n}^2\left[1 - \left(\frac{m_1 t_0}{m_0 t_1}\right)^2\right] &= n_1^2 - n_0^2\left(\frac{m_1 t_0}{m_0 t_1}\right)^2
\end{aligned}$$

Implying that the $\tilde{n}$-coordinate of the intersection point is:

$$\tilde{n} = \sqrt{\frac{n_1^2 - n_0^2\eta^2}{1 - \eta^2}} \tag{3.19}$$

where $\eta = (m_1/m_0)(t_0/t_1)$.

The intersection point of arbitrary $\tilde{n}_{m_1}(k)$ (high-index) and $\tilde{n}_{m_0}(k)$ (low-index) curves is thus found to be:

$$P_{(m_1,m_0)} \equiv (k,\tilde{n})|_{\tilde{n}_{m_1}=\tilde{n}_{m_0}} = \left(\pi\sqrt{\frac{1}{n_1^2-n_0^2}\left(\frac{m_1^2}{t_1^2}-\frac{m_0^2}{t_0^2}\right)}, \sqrt{\frac{n_1^2-n_0^2\eta^2}{1-\eta^2}}\right), \qquad (3.20)$$

These points thus form the corners of the aforementioned bound regions for a particular gap, and are here referred to as the *bounding points*.

Of particular note is that this expression for P is fully analytic in that each coordinate is independent of the other and a function of only the layer parameters n_i and t_i and mode orders m_i. This is entirely due to the analyticity of the SPARROW curves in which the transcendental Goos-Hänchen phase shift does not appear, as discussed above and in § A.2.1.2.

Note that this expression for the form of the bounding point P in Eq. 3.20 is invariant under the symmetry transform $1 \leftrightarrow 0$, as should be expected; the intersection between two curves is invariant to the order in which the curves are considered. Note that this does *not* imply that $P_{ab} \equiv P_{ba}$, since *all* indexed values are swapped (n_i, t_i, etc.) under the transform $1 \leftrightarrow 0$, not just the values of m_1 and m_0 which the subscripts of P_{ab} refer to. For example, by the definition of Eq. 3.20, the intersection point $P_{3,5}$ of bounding curves $\tilde{n}_{m_1=3}$ and $\tilde{n}_{m_0=5}$ is quite distinct from the intersection point $P_{5,3}$ of bounding curves $\tilde{n}_{m_1=5}$ and $\tilde{n}_{m_0=3}$, since only the mode indices have been swapped, not the layer types as is done under the $1 \leftrightarrow 0$ transform.

Since the $\tilde{n}_{m_i}(k)$ curves monotonically approach asymptotes at n_i ($\tilde{n}_{m_i} \to n_i$ as $k \to \infty$), all bound regions (hence bandgaps) will have a *maximal bounding point*: the intersection point whose k and $\tilde{n}$ values are larger than those of all other bounding points for that region. The maximal bounding point for a given bound region is thus the top-right bounding point when represented on a $(\Lambda/\lambda, \tilde{n})$ plot. Since the maximal bounding point exists for all gaps for all cladding configurations by construction, it may be used to define a consistent nomenclature for arbitrary bandgap spectra. Here one adopts the convention that each bound region or gap is referred to by the mode orders of the bounding curves producing the maximal bounding point. Explicitly, an arbitrary bound region is labelled as the $\langle m_1, m_0\rangle$ region. Some examples of how this nomenclature can be used to classify subsets of types of bound regions and their properties:

- the lowest order (fundamental) bound region (housing the fundamental bandgap) is labelled $\langle m_1, m_0\rangle = \langle 1, 0\rangle$ (using the § 3.4 definition that $m_0 = 0$ corresponds to the n_0-light-line),
- any region bound above by the $\tilde{n} = n_0$ line is an $\langle m_1, 0\rangle$ region or gap,

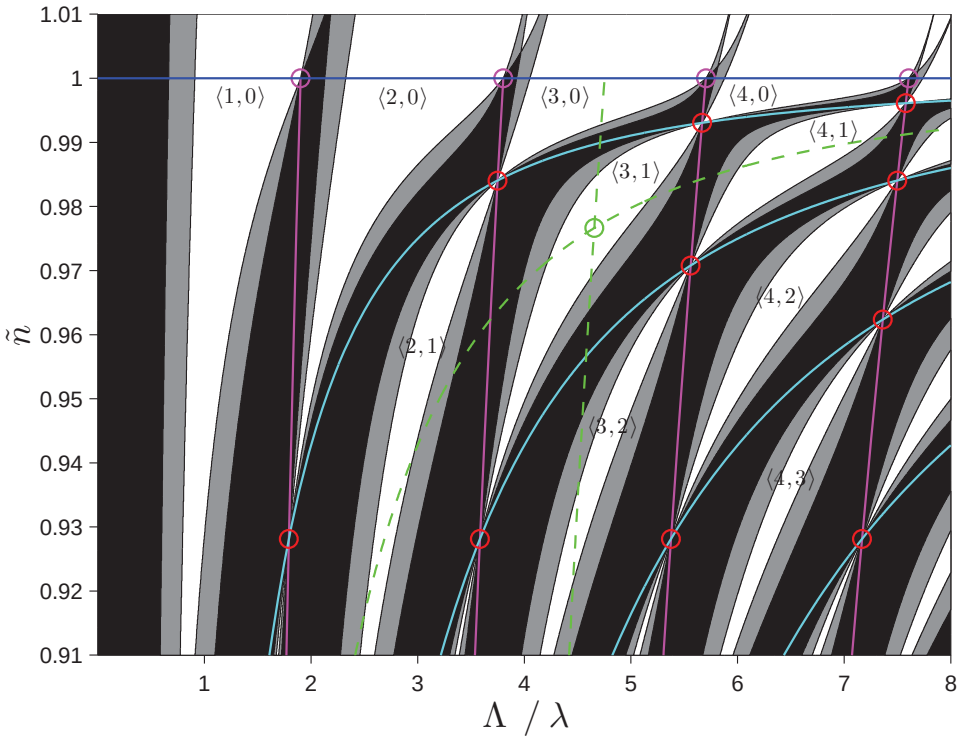

FIGURE 3.8: SPARROW model curves overlayed upon a portion of the cladding Bandgap map of the Bragg fibre examined in [43] and [147]: $t_1 = 0.37$ μm, $t_0 = 4.1$ μm, $n_1 = 1.45$ and $n_0 = 1$. The color scheme is the same as for Figs. 3.3 and 3.4. The bandgaps are labelled according to the nomenclature introduced in § 3.7.1. *Red circles*: intersection points (P, § 3.7.1) of the SPARROW curves. *Magenta circles*: $\tilde{n} = n_0$ resonances (Eqs. 3.2 and A.100). *Green dashed curves*: a specific bandgap's half-order curves, the intersection of which form P_c (§ 3.7.4), the *green circle*. The chosen gap is of order $\langle m_1, m_0 \rangle = \langle 3, 1 \rangle$ with $P_c = (k_c, \tilde{n}_c) \approx (5.34898\ \mu\text{m}^{-1}, 0.976641)$.

- if the $\langle m_1, m_0 \rangle|_{m_0>0}$ bound region exists, its maximal bounding point will be the lowest bounding point (in both $\tilde{n}$ and k) of the adjacent $\langle m_1 + 1, m_0 - 1 \rangle$ bound region. Associating this with the equivalent enclosed bandgaps in each bound region, this implies the $\langle m_1, m_0 \rangle$ bandgap closes up and opens again as the $\langle m_1 + 1, m_0 - 1 \rangle$ gap, as shown in Fig. 3.3 and discussed in §§ 3.4 and 3.5.

The bandgaps shown in Figs. 3.7 and 3.8 are labelled using this convention. It should be noted that this nomenclature is different (and more general) than that previously proposed by the authors in [147]. While that particular nomenclature was suitable for the particular fibre parameters examined, the system introduced here (and in the associated publication [61]) is more general and suitable for all conceivable configurations and regimes; due to the fact that the $\langle m_1, m_0 \rangle$ nomenclature here is based on a feature common to all bound regions [the maximal bounding point $P_{(m_1, m_0+1)}$].

Using this nomenclature, one can now quantify that the portions of the $\langle m_1, m_0 \rangle$ gap that close up within the $0 < \tilde{n} < n_0$ region will do so at the intersection points $P_{(m_1, m_0)}$

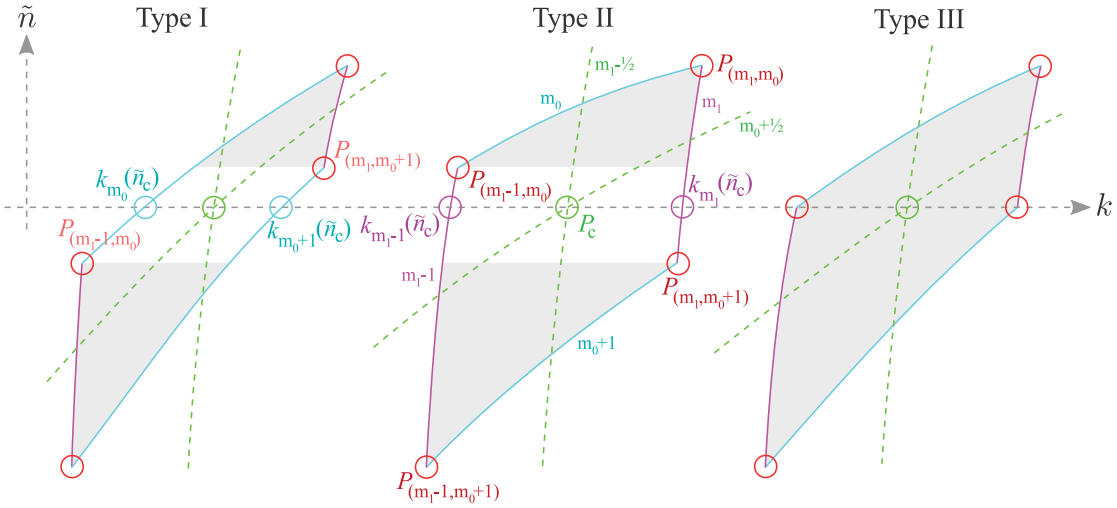

FIGURE 3.9: Schematic representation of the three fundamental types of SPARROW bound regions and their bounding points, complete with curve and intersection point labels. Each type differs only in their relative values of the $\tilde{n}$ components of the bounding points $P_{(m_1-1,m_0)}$ and $P_{(m_1,m_0+1)}$. See text for details.

and $P_{(m_1-1,m_0+1)}$, should these points exist within the domain for the given gap. If these points don't exist, the gap must then be terminated by the $\tilde{n} = 0$ or n_0 lines, leaving it open (seen explicitly in Figs. 3.4 and 3.8). Incidentally, it is likely that this gap closure behaviour explains the mode suppression phenomena observed in Ref. [201].

It should be noted here that during the completion of this thesis, a paper was published (April 2010) by Hsueh, Wun and Yu [202] (based upon an earlier work of Nusinsky and Hardy [203]) in which a they detailed a numerical technique quite similar to the SPARROW model and its ability to predict gap-closure points, but not from an antiresonance perspective (indeed, they make no mention of it) so much as a Bloch wave based analysis. Unfortunately, they appear to have neglected the SPARROW publication [61]. Nonetheless, their work goes further to establish how the antiresonance conditions (although, again, they make no allusion to the antiresonance mechanism explicitly) analytically satisfy the full Bloch wave gap closure points—although they use a structure scaling approach, not a frequency scaling one as done here. This is a direct formal validation of the reason for why the SPARROW model can be used in the ways described herein, building upon the phenomenological argument given in this Chapter.

3.7.2 The Antiresonance Mean Point

From Eq. A.100 the antiresonance mean point $\overline{k}_c$ is defined, at arbitrary $\tilde{n} = \tilde{n}'$, as the arithmetic mean of the bounding curve values $k_{m_i}(\tilde{n}')$ either side of the bound region (the central k value):

$$\overline{k}_c(\tilde{n}') = \tfrac{1}{2}\left[k_{m_p}(\tilde{n}') + k_{m_q}(\tilde{n}')\right], \tag{3.21}$$

where p and q refer to the adjacent bounding curve types in the k-dimension and m_q and m_p to their order, *i.e.*, $p, q \in \{1, 0\}$ and $m_p, m_q \in \mathbb{Z}^+$.

The nature of the adjacent curves in the definition of $\overline{k}_c$ depends upon the *type* of bound region considered and where within the region $\tilde{n}'$ sits. Three types of closed bound regions have been identified for a given $\langle m_1, m_0 \rangle$:

$$\begin{aligned}
\text{Type I:} \quad & \tilde{n}|P_{(m_1-1,m_0)} < \tilde{n}|P_{(m_1,m_0+1)} \\
\text{Type II:} \quad & \tilde{n}|P_{(m_1-1,m_0)} > \tilde{n}|P_{(m_1,m_0+1)} \\
\text{Type III:} \quad & \tilde{n}|P_{(m_1-1,m_0)} = \tilde{n}|P_{(m_1,m_0+1)},
\end{aligned}$$

summarised in Fig. 3.9.

The bound regions of each type can be divided into three sections: a top, middle and bottom. In Fig. 3.9, the top and bottom sections are represented as grey patches, and the middle section as white. The top section is the part of the region between the maximal bounding point $P_{(m_1,m_0+1)}$ and the next lowest bounding point in the $\tilde{n}$-dimension. The bottom section is the part of the region between the lowest two bounding points in the $\tilde{n}$-dimension. The middle section is the part of the region between the middle two bounding points $P_{(m_1-1,m_0)}$ and $P_{(m_1,m_0+1)}$. The precise points (and their order) defining each section depends on the region type. The adjacent mode orders required for the evaluation of $\overline{k}_c$ are now given for each section of each region type.

Type I

$$\begin{aligned}
\textit{Top section:} \quad & \tilde{n}|P_{(m_1,m_0+1)} \leq \tilde{n}' \leq \tilde{n}|P_{(m_1,m_0)} \\
& \Rightarrow\ m_p = m_1 \text{ and } m_q = m_0, \\
\textit{Bottom section:} \quad & \tilde{n}|P_{(m_1-1,m_0+1)} \leq \tilde{n}' \leq \tilde{n}|P_{(m_1-1,m_0)} \\
& \Rightarrow\ m_p = m_1 - 1 \text{ and } m_q = m_0 + 1, \\
\textit{Middle section:} \quad & \tilde{n}|P_{(m_1-1,m_0)} \leq \tilde{n}' \leq \tilde{n}|P_{(m_1,m_0+1)} \\
& \Rightarrow\ m_p = m_0 \text{ and } m_q = m_0 + 1.
\end{aligned}$$

Type II

$$\begin{aligned}
\textit{Top section:}\quad & \tilde{n}|P_{(m_1-1,m_0)} \leq \tilde{n}' \leq \tilde{n}|P_{(m_1,m_0)} \\
& \Rightarrow\ m_p = m_1 \text{ and } m_q = m_0, \\
\textit{Bottom section:}\quad & \tilde{n}|P_{(m_1-1,m_0+1)} \leq \tilde{n}' \leq \tilde{n}|P_{(m_1,m_0+1)} \\
& \Rightarrow\ m_p = m_1 - 1 \text{ and } m_q = m_0 + 1, \\
\textit{Middle section:}\quad & \tilde{n}|P_{(m_1,m_0+1)} \leq \tilde{n}' \leq \tilde{n}|P_{(m_1-1,m_0)} \\
& \Rightarrow\ m_p = m_1 - 1 \text{ and } m_q = m_1.
\end{aligned}$$

Type III Type III can be considered as either Type I or II for the top and bottom sections in this case since the intersection points lie on the same $\tilde{n}'$ (being a special case of both types above). The middle section is singular due to the level bounding points and can hence be considered non-existent.

The remaining types of regions are those that are terminated by the physical boundaries for guidance below the low-index light-line, namely the lines defined by: $\tilde{n} = n_0$ (the low-index light line—*e.g.*, glancing incidence in a level core), $\tilde{n} = 0$ (normal incidence), and $k = 0$ (infinite wavelength limit). Regions terminated by any of these boundaries can be considered variations of one of the above types except that the boundary line is dominant. The definition of the SPARROW model in § 3.4 defined the $\tilde{n} = n_0$ and $k = 0$ lines as corresponding to SPARROW curves with $m_0 = 0$ and $m_1 = 0$, respectively. These definitions ensure that the parameterisations of the SPARROW model results are consistent, and are highlighted as such where relevant.

Note how the bandgaps associated with the regions terminated by the $\tilde{n} = n_0$ and $\tilde{n} = 0$ lines remain open, Figs. 3.4 and 3.8. Of particular note is the former case since the gap edges are those terminated by the low-index light-line correspond only to high-index layer resonances, since the low-index layer modes are asymptotic to the $\tilde{n} = n_0$ line and hence can't intercept it. The fact that only the high-index resonances dominate there explains to some degree why the $\langle m_1, 0\rangle$ gaps are typically wider than those at lower $\tilde{n}$: the low-index resonances can only interrupt the bound regions (hence gaps) for regions below the low-index light-line.

To demonstrate the efficacy of the antiresonance mean point, Figure 3.7 demonstrates how $\overline{k}_c$ naturally predicts the approximate position of lowest CL for a core mode of the fibre discussed in § 3.6. The reason CL reaches a minimum near $\overline{k}_c$ follows directly from the findings of § 3.5 where it was shown how the reflectance from the layers is maximum in between the individual layer resonances; at $\overline{k}_c$, the guided wave is approximately maximally antiresonant with the pair of layers which produce the bounding dispersion curves

(of order m_p and m_q). Essentially, as one or the other bounding curve is approached, the guided wave becomes more resonant with the associated layer which allows greater out-coupling of the light from the core through the cladding (*i.e.*, the reflectance of the cladding is reduced—§ 3.5).

This is why the resonances of all layer types must be considered *together*, rather than separately, as discussed earlier, and is inherent in the definition of $\overline{k}_c$. The antiresonance mean point is thus a powerful tool for binary layered waveguide design and analysis, allowing immediate determination of the approximate point of minimum CL at arbitrary $\tilde{n}$ within an arbitrary region of the band map.

Note that, due to the analyticity of Eq. 3.21, the derivatives of $\overline{k}_c$ with respect to all waveguide parameters ($\partial\overline{k}_c/\partial n_i$, $\partial\overline{k}_c/\partial t_i$, etc.) can be easily derived. Such expressions would be ideal for the direct calculation of fabrication tolerances in waveguide design or sensitivities to core materials for sensing, for example.

3.7.3 Special Cases

There are two important special cases of the SPARROW model: $\tilde{n} = n_0$ and $\tilde{n} = 0$.

It is easily shown that the former case actually reduces the SPARROW model to the large-core limit of the Duguay-ARROW model, since by setting $i = 1$ (high-index layer) and $\tilde{n}_{m_1} = n_0$ in Eq. A.99 one derives Eq. 3.2. These $\tilde{n} = n_0$ resonances are shown in Fig. 3.8 (magenta circles); such resonances would be accessible predominantly to large core level-core waveguide structures in which $\tilde{n} \approx n_0$, as demonstrated by Fig. 2.8 in which the Duguay-ARROW type resonances (magenta circles) are overlayed on the bandgap map of the (level-core) idealised air-Bragg fibre analysed in Chapter 2. Thus, the SPARROW model also explains why the Duguay-ARROW model in the large-core regime (Litchinitser et al. [101]) is typically independent of the thickness of the low-index region as discussed in § 1: all orders of the low-index slab dispersion curves ($\tilde{n}_{m_0}$) have an asymptote at $\tilde{n} = n_0$ and hence never intercept it; their resonant features can never appear on the n_0-light-line (the region of applicability of Eq. 3.2).

The other special case, $\tilde{n} = 0$ (the zero-line), is derived in much the same way. However, in this case, both high- and low-index curves intercept the zero-line. Setting $\tilde{n}_i = 0$ one derives:

$$\lambda_{m_i} = \frac{2n_i t_i}{m_i} \tag{3.22}$$

where $i \in \{1, 0\}$. $\tilde{n} = 0$ corresponds to rays normally incident to the layered cladding since $\tilde{n} = n_i \sin(\theta_i) = 0$ for $\theta_i = 0$ (normal incidence).

The knowledge of these points is important for any practical implementation of the SPARROW model since they define the bounding points of bound regions terminating on the $\tilde{n} = n_0$ and $\tilde{n} = 0$ lines. Beyond use for the SPARROW model itself, these special cases occupy quite distinctly different regimes. The importance of the (Duguay-ARROW type) $\tilde{n} = n_0$ resonances for theoretical understanding of level-core antiresonant guidance and waveguide design is clear and has been discussed at length above. The $\tilde{n} = 0$ resonances, however, are less obvious in their utility beyond the SPARROW model. Normal incidence is an important regime for multilayer optical structures, particularly for high- or anti-reflection coatings, or for high-order modes within Bragg fibres [63]. However, for the infinite Bragg stack case, the Bloch band-edges themselves can be solved for relatively easily by enforcing $\tilde{n} = 0$ in the Bloch wave existence condition $\mathrm{Re}(M_{11}) \leq 1$, §§ 3.5 and A.3.2, which provide a more precise location of the high-reflectance regions of the stack than the individual layer resonances.

While useful in themselves, these two special cases reveal important information about the structure and topology of the antiresonance and Bandgap map. A more general consideration in § 3.7.5 develops this further, providing analytical expressions describing the general topology of the SPARROW and bandgap spectrum.

3.7.4 The Central Antiresonance Point

The concept of the *central antiresonance point* can now be introduced: the points on the $(\tilde{n}, \Lambda/\lambda)$ at which both cladding layer types are antiresonant.

Note that the slab dispersion curves with half-orders $(\frac{1}{2}, \frac{3}{2}, \frac{5}{2}, \ldots)$ fall mid-way between adjacent integer-order curves for both $i = \{1, 0\}$ in both the k and $\tilde{n}$ dimensions. An example is shown in Fig. 3.8 (green dotted curves). Thus, I define the central antiresonance point as the intersection point of the half-order curves within a particular gap, naturally defining the point at which both layer types are antiresonant.

Using the nomenclature defined in § 3.7.1, the curves producing the central antiresonance point for the $\langle m_1, m_0 \rangle$ gap are the $m_1^{'} = m_1 - \frac{1}{2}$ and $m_0^{'} = m_0 + \frac{1}{2}$ curves, so that the position of the gap's center is given a modified form of Eq. 3.20 where $m_1 \rightarrow m_1 - \frac{1}{2}$ and $m_0 \rightarrow m_0 + \frac{1}{2}$, namely:

$$\begin{aligned} P_c \equiv & (k_c, \tilde{n}_c) \equiv P_{(m_1 - \frac{1}{2}, m_0 + \frac{1}{2})} \\ = & \left(\pi \sqrt{\frac{1}{n_1^2 - n_0^2} \left[\left(\frac{m_1 - \frac{1}{2}}{t_1} \right)^2 - \left(\frac{m_0 + \frac{1}{2}}{t_0} \right)^2 \right]}, \sqrt{\frac{n_1^2 - n_0^2 \eta_c^2}{1 - \eta_c^2}} \right), \end{aligned} \tag{3.23}$$

where $\eta_c = \frac{(m_1-\frac{1}{2})t_0}{(m_0+\frac{1}{2})t_1}$. An example based on the fibre cladding examined in [43, 147] is shown in Fig. 3.8, where $P_c = P_{(\frac{5}{2},\frac{3}{2})} \approx (5.34898\ \mu\text{m}^{-1}, 0.976641)$ (green circle) corresponding to the $\langle 3,1\rangle$ gap.

In fact, P_c is formally compatible with the antiresonance mean point ($\overline{k}_c$) of Eq. 3.21 such that:

$$\overline{k}_c(\tilde{n}_c) = k_c. \tag{3.24}$$

This is not at all obvious at first glance. The proof for Eq. 3.24 follows.

Proof:

For a Type I bound region (Fig. 3.9), the antiresonance mean point expression from Eq. 3.21 implies:

$$\begin{aligned}\overline{k}_c(\tilde{n}_c) =& \tfrac{1}{2}\left[k_{m_0}(\tilde{n}_c) + k_{m_0+1}(\tilde{n}_c)\right]\\ =& \frac{m_0\pi}{2t_0}\left(n_0^2-\tilde{n}_c^2\right)^{-\frac{1}{2}} + \frac{(m_0+1)\pi}{2t_0}\left(n_0^2-\tilde{n}_c^2\right)^{-\frac{1}{2}}\\ =& \frac{(m_0+\frac{1}{2})\pi}{t_0}\left(n_0^2-\tilde{n}_c^2\right)^{-\frac{1}{2}}.\end{aligned} \tag{3.25}$$

But from the definition of $\tilde{n}_c$ (Eq. 3.23), the argument of the $(\ldots)^{-\frac{1}{2}}$ factor can be evaluated as:

$$n_0^2 - \tilde{n}_c^2 = n_0^2 - \frac{n_1^2 - n_0^2\eta_c^2}{1-\eta_c^2} = \frac{n_0^2-n_1^2}{1-\eta_c^2}, \tag{3.26}$$

so that:

$$\overline{k}_c(\tilde{n}_c) = \frac{(m_0+\frac{1}{2})\pi}{t_0}\sqrt{\frac{1-\eta_c^2}{n_0^2-n_1^2}}. \tag{3.27}$$

Now, note that also from the definition of $\tilde{n}_c$ (Eq. 3.23):

$$n_1^2 - \tilde{n}_c^2 = n_1^2 - \frac{n_1^2 - n_0^2\eta_c^2}{1-\eta_c^2} = \eta_c^2\frac{n_0^2-n_1^2}{1-\eta_c^2}, \tag{3.28}$$

such that one can use the expression for the high-index half-order antiresonance curves ($k_{m1=\frac{1}{2},\frac{3}{2},\ldots}$ via Eq. A.100) to express k_c as:

$$\begin{aligned}k_c(\tilde{n}_c) =& \frac{(m_1-\frac{1}{2})\pi}{t_1}\left(n_1^2-\tilde{n}_c^2\right)^{-\frac{1}{2}}\\ =& \frac{(m_1-\frac{1}{2})\pi}{t_1}\frac{1}{\eta_c}\sqrt{\frac{1-\eta_c^2}{n_0^2-n_1^2}}\\ =& \frac{(m_0+\frac{1}{2})\pi}{t_0}\sqrt{\frac{1-\eta_c^2}{n_0^2-n_1^2}}\\ =& \overline{k}_c(\tilde{n}_c),\end{aligned} \tag{3.29}$$

where Eqs. 3.28 and 3.27 have been used at the second and final steps, respectively. This proves Eq. 3.24 for Type I bound regions. This last step can also be derived by manipulating the form of k_c from Eq. 3.23 directly.

For a Type II bound region (Fig. 3.9), the antiresonance mean point expression from Eq. 3.21 implies:

$$\begin{aligned}
\overline{k}_c(\tilde{n}_c) =& \tfrac{1}{2}\left[k_{m_1}(\tilde{n}_c) + k_{m_1-1}(\tilde{n}_c)\right] \\
=& \frac{m_1\pi}{2t_1}\left(n_1^2 - \tilde{n}_c^2\right)^{-\frac{1}{2}} + \frac{(m_1-1)\pi}{2t_1}\left(n_1^2 - \tilde{n}_c^2\right)^{-\frac{1}{2}} \\
=& \frac{(m_1-\frac{1}{2})\pi}{t_1}\left(n_1^2 - \tilde{n}_c^2\right)^{-\frac{1}{2}} \\
=& \frac{(m_1-\frac{1}{2})\pi}{t_1}\frac{1}{\eta_c^2}\sqrt{\frac{1-\eta_c}{n_1^2-n_0^2}} \\
=& \frac{(m_0+\frac{1}{2})\pi}{t_0}\sqrt{\frac{1-\eta_c^2}{n_1^2-n_0^2}},
\end{aligned} \tag{3.30}$$

where Eq. 3.28 has been used at the fourth step. One can use the expression for the low-index half-order antiresonance curve ($k_{m0=\frac{1}{2},\frac{3}{2},\ldots}$ via Eq. A.100) to express k_c as:

$$\begin{aligned}
k_c(\tilde{n}_c) =& \frac{(m_0+\frac{1}{2})\pi}{t_0}\left(n_0^2 - \tilde{n}_c^2\right)^{-\frac{1}{2}} \\
=& \frac{(m_0+\frac{1}{2})\pi}{t_0}\sqrt{\frac{1-\eta_c^2}{n_0^2-n_1^2}} \\
=& \overline{k}_c(\tilde{n}_c),
\end{aligned} \tag{3.31}$$

where Eqs. 3.26 and 3.30 have been used at the second and final steps, respectively. This proves Eq. 3.24 for Type II bound regions. This last step can also be derived by manipulating the form of k_c from Eq. 3.23 directly.

The proof for Type III bound regions follows immediately from those for Type I and II since the former can be considered as either one or other of the latter for this purpose.

QED

Since the gaps bound by the $\tilde{n} = n_0$ and/or $\tilde{n} = 0$ lines are open (above and below, respectively), this definition of the center point is insufficient when P_c reaches these lines, or where P_c simply doesn't exist (as is the case for all $\langle m_1, 0\rangle$ gaps). In these cases, the antiresonance mean point (Eq. 3.21) is used to define $P_c = (\overline{k}_c(\tilde{n}'), \tilde{n}')$ where $\tilde{n}' = n_0$ or 0 as appropriate. Thanks to Eq. 3.24, this gap center formalism is thus consistent for all bandgaps.

It is expected that P_c will determine the approximate point of lowest modal CL for a given bandgap in not just the k-dimension (via the relation to $\overline{k}_c$ from Eq. 3.24) but also the $\tilde{n}$-dimension. This is to be expected from the work of [63], where it was demonstrated that as the bandgap edges are approached from any direction, CL generally increases. Since P_c dictates the point at which light is maximally antiresonant with both cladding layer types, it is reasonable to expect that the CL is thus minimum near this point. While omitted here for brevity, a quantitative verification of this would be straightforward, requiring the CL spectra of the modes of interest to be calculated for a range of $\tilde{n}$. This could be achieved by iterating the spectral analysis (via a FEM as in § 3.6, for example) over a range of n_{core} to generate modes within the entire domain of the bandgap of interest (*i.e.*, to calculate CL in both the k- and $\tilde{n}$-dimensions).

Also, similar to the discussion of § 3.7.2, the derivatives of P_c with respect to all cladding parameters ($\partial k_c/\partial n_i$, $\partial k_c/\partial t_i$, $\partial \tilde{n}_c/\partial n_i$ and $\partial \tilde{n}_c/\partial t_i$) can also be easily derived, and would also be ideal for similar applications.

3.7.5 Bandgap Topology and the Bound Region

Here another powerful feature of the SPARROW model is derived: the determination of the topology of an arbitrary 1-D stack's antiresonance (and equivalently, bandgap) spectrum via a simple analytic expression. That is, it can be used to determine the number of bandgaps in a given region and how they join together.

Eq. 3.20 can be used to determine the number of bandgaps (or more precisely, bound regions) that exist between a pair of adjacent high-index slab curves, $n_{m_1}(k)$, which have orders $m_1 - 1$ (left curve in the k-dimension) and m_1 (right curve). The domain enclosed by this curve pair and the $\tilde{n} = n_0$ and $\tilde{n} = 0$ lines is denoted D_{m_1}. Insofar as a correlation with antiresonance and bandgap behaviour is concerned (as discussed above), this analysis pertains to only TE bandgaps directly. Extension to TM gaps is trivial since they have the same topology as the TE gaps save for the gap closure induced by the Brewster condition at $\tilde{n} = \tilde{n}_{\text{B}}$ (§ 2.3.2, Figs. 3.3, 3.4 and 3.8).

It is easy to see from Fig. 3.10 (and Figs. 3.3 and 3.4) that the number of bound regions, hence TE gaps, within D_{m_1} is one greater than the number of intersection points made by the low-index curves $[n_{m_0}(k)]$ with the rightmost bounding curve $[n_{m_1}(k)]$, excluding the n_0-light-line ($m_0 = 0$). To show this analytically, one must enforce upon the intersection point expression (Eq. 3.20) the physical condition: $P_{(m_1,m_0)} \in \mathbb{R}^2$. By enforcing $k \in \mathbb{R}$, the square-root requires $(m_1/t_1)^2 - (m_0/t_0)^2 > 0 \Rightarrow \eta > 1$ (where η is defined with Eq. 3.20). This can be used to find an upper limit $m_0 < m_1(t_0/t_1)$, but a more strict limit is found by enforcing the second physical condition $\tilde{n} \in \mathbb{R}$: since

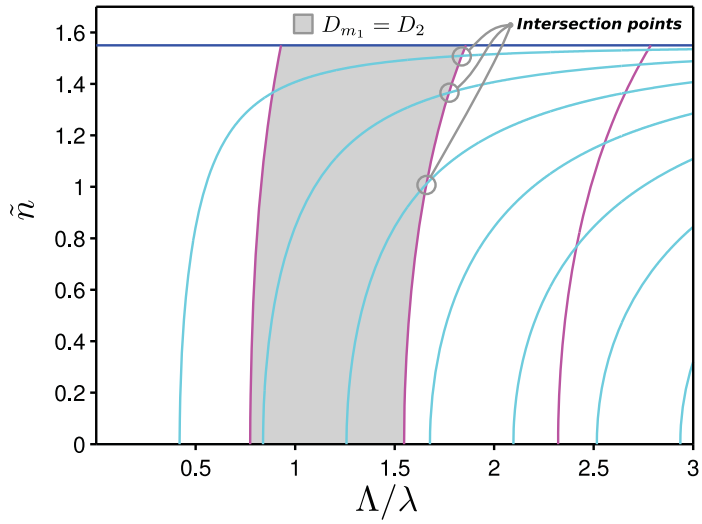

FIGURE 3.10: An example of antiresonance and bandgap map topology via the SPARROW model. The SPARROW curves shown here are those shown in Figs. 3.3 and 3.4. The shaded region represents the second D_{m_1} domain, D_2. The circles highlight the intersection points of the high-order high-index bounding curve $\tilde{n}_{m_1=2}(\Lambda/\lambda)$ with all low-index curves $\tilde{n}_{m_0=1,2,3}(\Lambda/\lambda)$ passing through D_2. There are thus $N_2 = 3$ intersection points and $N_2 + 1 = 4$ bounded regions, as per the text.

$\eta > 1$, $1 - \eta^2 < 1$ so that the numerator (within the square-root) must also be negative: $n_1^2 - n_0^2\eta^2 < 1 \Rightarrow n_1/n_0 < \eta$. This last inequality gives the most strict range physically imposed on m_0, namely:

$$m_0 < m_1 \frac{n_0 t_0}{n_1 t_1}. \tag{3.32}$$

Thus, the maximum permissible order of an m_0-curve within D_{m_1} is:

$$m_0^{\max} = \text{floor}\left\{ m_1 \frac{n_0 t_0}{n_1 t_1} \right\}, \tag{3.33}$$

which is also the number of m_0-curves within D_{m_1} (excluding the $\tilde{n} = \{0, n_0\}$ lines). The number of TE bandgaps within D_{m_1} is thus $m_0^{\max} + 1$; the '+1' accounting for the ever present $\langle m_1, 0\rangle$ gaps, bound above by the n_0-light-line, whose maximal bounding point $P_{(m_1,0)}$ doesn't contribute to $m_0^{\max}$ by definition, as discussed.

There is an exception to this analysis: where a maximal bounding point lies *on* the zero-line ($\tilde{n} = 0$) such that the point exists but the associated gap does not (the bound region becomes singular). In this case, the number of gaps within D_{m_1} is exactly equal to the number of intersection points on $\tilde{n}_{m_1}(k)$ (including the $\tilde{n} = 0$ bounding point). Quantitatively, the condition for this behaviour can be deduced from the SPARROW model's $\tilde{n} = 0$ special case (Eq. 3.22) by setting $\lambda_{m_1} = \lambda_{m_0}$, demonstrating that the above inequality (Eq. 3.32) becomes an *equality* (*i.e.*, the floor function of Eq. 3.33 becomes redundant).

One can thus express the total number of gaps bound within D_{m_1} as:

$$N_{m_1} = \begin{cases} m_0^{\max} + 1 & \text{when } m_0^{\max} < m_1 \frac{t_0 n_0}{t_1 n_1} \\ m_0^{\max} & \text{when } m_0^{\max} = m_1 \frac{t_0 n_0}{t_1 n_1} \end{cases} \tag{3.34}$$

which depends only upon the cladding parameters and just one order parameter, m_1 (required to define D_{m_1}).

The only difference in topology for the TM gaps over the TE gaps is that the Brewster-induced gap closure increases the number of gaps within D_{m_1} by 1 (*i.e.*, $N_{m_1} + 1$), the position of the extra closure being $\tilde{n} = n_{\mathrm{B}}$ (§§ 2.3.2 and A.3.2). The only exception is when n_{B} coincides with a TE gap closure point, $P_{(m_1,m_0)}$, in which case the associated TM gap's bound region becomes singular (similar to the P_c at $\tilde{n} = 0$ case above) and the number of gaps within D_{m_1} is identical to the TE case (*i.e.*, N_{m_1}).

The above expressions for the intersections points (Eq. 3.20) and the number of gaps within a given domain D_{m_1} (Eq. 3.34) explicitly define the topology for any given bandgap spectrum: the number of gaps (in a finite domain) and how they join together.

Figure 3.4 gives an explicit example of how a bandgap spectrum topology can change with varying cladding parameters. The top plot in the figure shows the bandgap map of Fig. 3.3 with the cladding layer dispersion (SPARROW) curves (Fig. 3.3) overlayed. The bottom plot of the figure shows the bandgap and SPARROW curves of the same cladding structure configuration but with the high-index layer's thickness decreased: $t_1 = 0.27\ \mu\mathrm{m} \rightarrow 0.18\ \mu\mathrm{m}$. The bandgap topology dramatically changes between the two cases with the bandgaps shifting with the layer resonances and, most importantly for here, new bandgaps created which alter the topology of the bandgap spectrum. Using the nomenclature and analysis just developed, number of gaps within a given domain can be easily evaluated. The first case ($t_1 = 0.27\ \mu\mathrm{m}$) produces $N_1 = 2$ bandgaps in the D_1 domain (the region bound by the $\tilde{n}_{m_1=2}$ curve and the $k = 0$ line—the $\tilde{n}$-axis) and $N_2 = 4$ bandgaps in the D_2 domain (bound by $\tilde{n}_{m_1=1}$ and $\tilde{n}_{m_1=2}$). By shrinking the high-index layer to $t_1 = 0.18\ \mu\mathrm{m}$, the number of gaps (equivalently, bound regions) in the respective domains becomes $N_1 = 3$ and $N_2 = 6$. The topology dramatically changes.

Considerations of resonance and bandgap topology are critical if one wishes to design a low-index core layered-cladding waveguide which exploits higher-order bandgaps.

3.8 Concluding Remarks

In this chapter, an intimate relationship between the bandgap and antiresonance pictures of light confinement in binary-layered-cladding waveguides on and *below* the low-cladding-index light-line was demonstrated. From this it was implied that Bragg fibres and Integrated-ARROWs guide by fundamentally the same principles. From these considerations, a novel antiresonance model was developed, the SPARROW model, that describes the resonances of an arbitrary waveguide's binary cladding layers independent of the core properties. The SPARROW model is a generalisation of the Archambault-ARROW model [174] in that the resonances of both high- and low-index layers are described but their resonant properties are considered as decoupled from those of the core. This decoupling permits the direct comparison of the layers' dispersive behaviour with the associated Bloch-wave bandgap spectra.

Foremost, the model demonstrates that the cladding layer dispersion curves replicate the nontrivial structure and topology of the analogous Bloch-mode bandgap spectrum for all $\tilde{n}$ on and below the light-line of the low-index cladding layer. By exploiting this, the model is also capable of quantitatively and analytically describing nontrivial features of such spectra. Among the most important features of the model derived were: a consistent nomenclature for arbitrary bandgap spectra ($\langle m_1, m_0 \rangle$); the approximate position of lowest core-mode confinement loss of any gap via the antiresonance mean point ($\overline{k}_c$); the precise closure points of a given gap ($P_{(m_1,m_0)}$ and/or $P_{(m_1-1,m_0+1)}$); the center of a gap in both $\tilde{n}$- and k-dimensions via the central antiresonance point (P_c); and the number of bandgaps within a specific domain (*e.g.*, N_{m_1} for TE), thus the bandgap spectrum topology; all via simple analytic expressions.

The SPARROW model is thus a powerful and simple tool for the spectral analysis and design of layered cladding dielectric waveguides with core refractive indices equal to or less than the lowest cladding index. Integrated-ARROWs have recently been demonstrated as ideal hollow-core waveguides for sensing and microfluidics [26–29, 56–59]. However, using the SPARROW model, an analysis of a liquid-core Bragg fibre was performed (and confirmed via a finite element model) implying that fibres hold similar promise. Indeed, recent literature [19] has highlighted the potential promise of Bragg fibres for sensing and microfluidics applications.

The hollow cores of Bragg fibres or Integrated-ARROWs could also be filled with active gain media (*e.g.*, Ref. [30]) to develop novel waveguide lasers or filled with other low-index media such as nonlinear liquids and gases for novel low-power nonlinear optical applications. The SPARROW model and the principles of, and relationships between,

their antiresonances and bandgap behaviours will simplify and give deeper insight into the design of such waveguides and their applications.

Of particular importance is the SPARROW model's ability to determine the aforementioned properties of *higher-order* resonances and bandgaps. Since many applications typically exploit the fundamental (or low-order) resonance(s) or bandgap(s), the existence of the rich topology of higher-order spectral features suggests great potential for novel extensions of the aforementioned applications.

This chapter also presented a thorough analytical analysis of the reflectance properties of binary stratified media with a finite number of layers. It was demonstrated how conditions for antiresonance, as per the SPARROW model, can be derived by minimising the reflectance functions of the layered structures. From this, physical insight into the connections between the antiresonance mechanism and multilayer reflectance was discussed. Extending upon this analysis, the evolution of the reflectance maps from few layers to many layers was demonstrated, indicating an evolution from the antiresonance to the bandgap regime. The implications for this behaviour were discussed both in terms of the connections between the antiresonance and bandgap mechanisms themselves and their relevance for practical multilayer waveguides.

The application of resonance analyses like the SPARROW model to more complicated structures, such as 2-D photonic crystals, could provide an interesting avenue for future work. As noted in Chapter 1, however, the bandgap spectra of such 2-D structures below the low-index light-line are less regular owing to the increased complexity in the Bloch wave behaviour sue to the inclusion of periodicity in 2 dimensions instead of only one. It was also discussed how the photonic tight-binding model, which considers only the Bloch modes on the edges of the Brillouin zone (and hence the most confined to the dominant structural features), can precisely describe such gap edges. The consideration of the resonance of an isolated resonator (dominant structural feature), rather than one coupled to neighbouring resonators, would likely make for a poor approximation to the required Bloch edges. Nonetheless, this is an area worthy of further study.

In the next chapter, the concept of resonance-based refractive index sensing is investigated experimentally by systematically filling the core of a Bragg fibre with liquids of various refractive indices—a clear connection with the results of this chapter is obvious. The shift of the transmission spectrum with respect to the core refractive index is measured and compared with the associated bandgap spectrum and the position of the core modes within it.

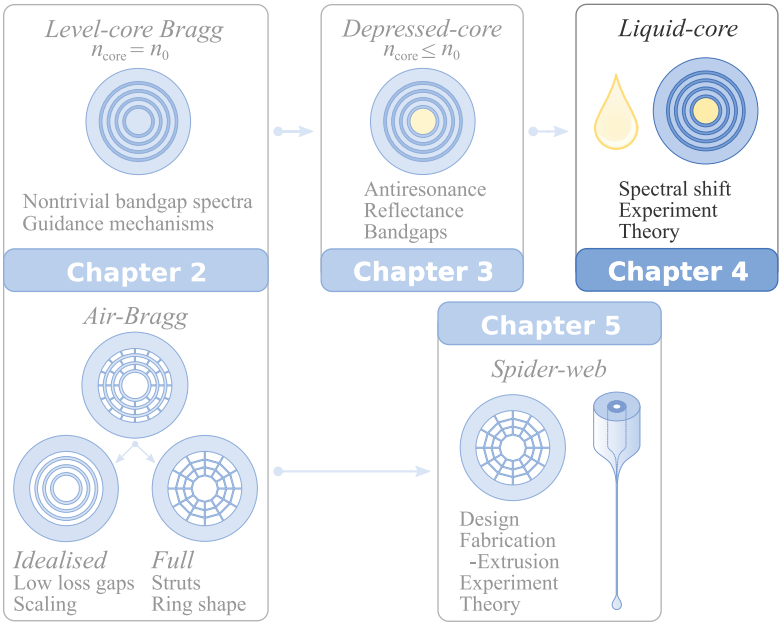
Level-core Bragg
$n_{core} = n_0$
Nontrivial bandgap spectra
Guidance mechanisms
Chapter 2
Depressed-core
$n_{core} \leq n_0$
Antiresonance
Reflectance
Bandgaps
Chapter 3
Liquid-core
Spectral shift
Experiment
Theory
Chapter 4
Air-Bragg
Idealised
Low loss gaps
Scaling
Full
Struts
Ring shape
Chapter 5
Spider-web
Design
Fabrication
-Extrusion
Experiment
Theory